PROPAGATION OF POLARIZED LIGHT IN SKELETAL MUSCLE

A Thesis presented to
the Faculty of the Graduate School
at the University of Missouri

In Partial Fulfillment of the Requirements for the Degree

Master of Science

---

by
XIN LI

Dr. Gang Yao, Thesis Supervisor

MAY 2009

The undersigned, appointed by the dean of the Graduate School, have examined the thesis entitle

PROPAGATION OF POLARIZED LIGHT IN SKELETAL MUSCLE

presented by Xin Li,

a candidate for the degree of Master of Science,

and hereby certify that, in their opinion, it is worthy of acceptance.

Gang Yao, Ph.D., Department of Biological Engineering

Jinglu Tan, Ph.D., Department of Biological Engineering

Ye Duan, Ph.D., Department of Computer Science

ACKNOWLEDGEMENTS

First of all, I would like to express my gratitude to my advisor Dr. Gang Yao who gave me the opportunity to extend my education and to study in the field of tissue optics. I thank him for all the support, professional guidance, and inspiration for future direction he provided. I have learned a lot from him on how to be an independent researcher, and what is dedication and diligence to the career of research. I also thank all my committee members: Dr. Jinglu Tan, and Dr. Ye Duan, for their advice in my research and thesis preparation.

I want to express my thanks to my former lab colleague Dr. Janaka C. Ranasinghesagara, for his stimulating advice and pleasant collaboration in research. Also, I want to thank my current colleagues Xiaofei Fan, Chuanmao Fan, Ali Shuaib and Chanthuri Daluwatte for their valuable help during my studies. I want to give special thanks to the meat lab manager Rick Disselhorst for his help of muscle sample extraction and Cliff Mongler for his patient help in the machine shop.

Finally, I want to thank my friends and family for their endless support and help during my two years' master study abroad. They always think at my side and give me great happiness and confidence.

TABLE OF CONTENTS

LIST OF FIGURES

Figure Page

LIST OF TABLES

PROPAGATION OF POLARIZED LIGHT IN SKELETAL MUSCLE

Xin Li

Dr. Gang Yao, Thesis Supervisor

ABSTRACT

Skeletal muscle is a very important tissue in animals and humans. Optical polarization imaging is a non-invasive method to study biological tissues and provides unique polarization contrast. An imaging system was developed to acquire optical polarization-sensitive images in muscles. Both reflectance and transmittance images were studied and compared with those images in isotropic scattering media.

In reflectance measurements, 16 raw polarization images were acquired. The Stokes images, Mueller matrix images and degree of polarization (DOP) images were calculated. Polar decomposition algorithms were applied to derive polarization parameters. We also studied the effects of muscle stretching. The equi-intensity profiles in the polarization images of muscle showed very distinguished patterns which had a preference across the muscle fiber direction. The single and double scattering models in isotropic media were applied to compare with the experimental results in polystyrene solution. Mie scattering theory can not explain all the experimental results observed in muscle. Using a diffraction model, the unique features shown in the Mueller matrix and DOP images of muscle can be explained as the sarcomere diffraction effect.

In the transmittance measurement, we acquired polarization images in samples of different thicknesses. The polarization intensity patterns were analyzed, and the Mueller matrix images were calculated. The intensity decay curve, DOP values, and the polar

decomposition parameters of the ballistic and scattering propagation regions were calculated. The results show that polarized light propagation through skeletal muscle is affected by the scatters in muscle, the fibrous structure in tissue, and the diffraction effect from the sarcomere structure.

Further studies are necessary to investigate how the skeletal muscle structure affects the polarized light propagation, and how to calculate and remove the effect of the skin and fat tissue for *in vivo* measurements.

CHAPTER 1

INTRODUCTION AND BACKGROUND

1.1 Research Topic and Objectives

Recently, light propagation in biological tissue has drawn much attention (Tuchin, *et al*., 2006) because of its potential as a noninvasive tool for disease diagnosis. Skeletal muscle is a very important tissue for producing force and motion. Each skeletal muscle consists of hundreds of thousands of muscle fibers and has optical anisotropic characteristics. The fundamental unit of skeletal muscle is sarcomere, a periodic repetitive structure that is responsible for contraction.

Using a non-ionizing radiation optical imaging method to study skeletal muscle structures has drawn interest in the academic field (Pasquesi, *et al*., 2006; Ranasinghesagara and Yao, 2007; Xia, *et al*., 2006; Zijp and ten Bosch, 1998). Reflectance and transmittance measurements are two important ways to study light propagation in scattering media. In this study, we investigated the polarization sensitive reflectance and transmittance imaging of skeletal muscles. We expect that these measurements can reveal the muscle structural information and may help us understand how light propagates in such a complicated tissue.

1.2 Introduction of Polarization Optics

1.2.1 Overview of Polarized light

From the classic physics point of view, light is a transverse electromagnetic wave which vibrates transversely to the propagation direction. Polarized light shows a preference of vibration, such as to the transverse direction or to the handedness associated direction.

The polarization of light was discovered by Erasmus Bortolinus in 1669. In 1928, Edwin Herbert Land invented the sheet-type polarizer (Shurcliff and Ballard, 1964). This invention had greatly impacted the scientific fields of physics, chemistry, biology, electronics engineering, and mechanical engineering, etc. Later, the tools of Stokes vector, the Mueller calculus and the Jones calculus were developed, which are powerful for predicting the effects of polarizer, retardation plates and so on. Besides being of a scientific interest for a long time in various fields, polarized light also serves as a useful tool or probe to evaluate the properties of different materials.

1.2.2 Polarization States of Optical Waves

As the electronic field vector of the polarized light oscillates in the plane perpendicular to the light propagation direction, it can be divided into two components perpendicular to each other. If these two components have the same phase, the electronic field vector will trace out a line within the plane. This special case is called linear polarization as is shown in Fig. 1-1(a). If these two components are different in the

attitude or the phase, the electronic field vector will trace out an ellipse in the plane, so this case is called elliptical polarization as shown in Fig. 1-1(c).

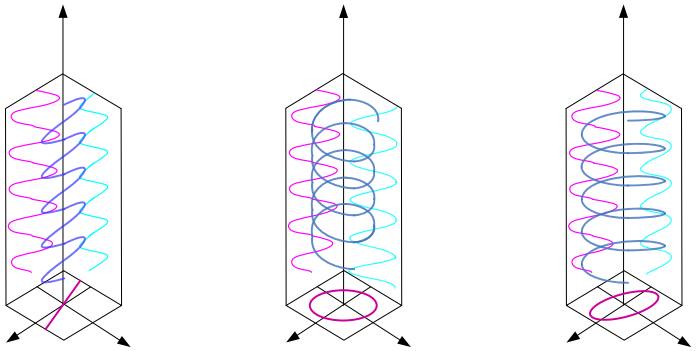

(a) (b) (c)

Fig. 1-1. Schematic of typical polarization states: (a) linear polarization, (b) circular polarization, and (c) elliptical polarization (Doit, 2006).

If the two components have the same attitude, and are exactly 90^o out of phase, the electronic field vector will trace out a circle in the plane, and this case is called circular polarization as shown in Fig. 1-1(b). It is a special case of elliptical polarization. The circular polarization can be further classified as right-handed circular polarization and left-handed circular polarization according to which way the electric vector rotates.

1.2.3 Representations of the State of Polarization

a. Stokes Parameters

The Stokes vector consists of four Stokes parameters which are based on the six flux measurements with different polarization analyzers in front of the detector. It can be applied to describe the intensity and polarization of a light. The Stokes parameters S_0, S_1, S_2 and S_3 are defined by following relations:

$$\begin{cases} S_0 = I_x + I_y \\ S_1 = I_x - I_y \\ S_2 = I_{+45^\circ} - I_{-45^\circ} \\ S_3 = I_R - I_L \end{cases} \tag{1-1}$$

It is obviously that S_0 represents the total intensity of the optical wave, and S_1 represents the intensity difference between the linear components polarized along x and y direction. Similarly, S_2 represents the intensity difference between the linear components polarized with $+45^o$ and -45^o to x axis; and S_3 represents the intensity difference between circular components of left-handed and right-handed direction.

The Stokes vector is a vector that gathers the four Stokes parameters together as a four-component array, as following:

$$S = \begin{bmatrix} S_0 \\ S_1 \\ S_2 \\ S_3 \end{bmatrix} = \begin{bmatrix} I_x + I_y \\ I_x - I_y \\ I_{+45^\circ} - I_{-45^\circ} \\ I_R - I_L \end{bmatrix} \tag{1-2}$$

b. Mueller Matrix

Mueller Matrix is a 4*4 matrix designed to describe an optical element that can change the light polarization state. For example, if a beam is initially in the state of S_i, after passing through an optical medium, it changes to the state of S_o:

$$S_o = \mathbf{M} S_i , \tag{1-3}$$

where M is the Mueller matrix of the medium.

c. Jones Representation

The Jones vector describes a polarized light in the algebraic form and is suitable to solve problems involving beams whose phase relations are important.

The Jones vector is defined by:

$$\mathbf{J} = \mathbf{E}(t) = \begin{bmatrix} E_x(t) \\ E_y(t) \end{bmatrix} = \begin{bmatrix} E_{0x} e^{i\phi x} \\ E_{0y} e^{i\phi y} \end{bmatrix} \tag{1-4}$$

Polarization states are orthogonal when $\mathbf{J_i} \cdot \bar{\mathbf{J}}_\mathbf{j} = 0$.

If an optical element is rotated about the optical axis by angle θ, the Jones matrix for the rotated element, M(θ), is constructed from the matrix for the unrotated element, M, by the transformation

$$\mathbf{M}(\theta) = \mathbf{R}(-\theta)\mathbf{M}\mathbf{R}(\theta), \tag{1-5}$$

where

$$\mathbf{R}(\theta) = \begin{pmatrix} \cos\theta & \sin\theta \\ -\sin\theta & \cos\theta \end{pmatrix}. \tag{1-6}$$

Jones calculus is only applicable to light that is fully polarized. Light which is unpolarized, partially polarized, or incoherent must be treated with Mueller calculus.

1.2.4 Degree of Polarization

The degree of polarization (DOP) is used to study the partially polarized light during light propagation. In the case of partial polarization, the Stokes vector can be described as Eq. 1-2, and the associated DOP can be described as following:

$$DOP = \frac{\sqrt{S_1^2 + S_2^2 + S_3^2}}{S_0}. \tag{1-7}$$

The value of DOP is between 0 and 1. A DOP = 0 indicates a fully unpolarized light, and a DOP = 1 indicates a fully polarized light. The light is partially polarized when DOP is between 0 and 1.

1.2.5 Polar Decomposition

Mueller matrix measurements are often used in biological optics applications (Bickel, *et al.*, 1976; Hielscher, *et al.*, 1997; Yao and Wang, 1999). Since the sixteen-element (4×4) Mueller matrix is difficult to interpret directly, decomposition methods have been explored to extract useful information from the full Mueller matrix measurements. Lu and Chipman (1996) introduced the polar decomposition method to derive the diattenuation, retardance, and depolarization matrices from a Mueller matrix. Swami *et al*. (2006) explored a simplified decomposition algorithm for use in a subset (3×3) of the Mueller matrix measured with only linearly polarized light. Manhas *et al*. (2006) and Ghosh *et al*. (2008) recently extended Lu and Chipman's original method by further decomposing the total retardance into linear retardance and optical rotation.

Several experimental studies have demonstrated the usefulness of such decomposition techniques in tissue characterization. Smith (2001) applied polar decomposition to analyze images of human skin with cancerous moles and Lupus lesions. His results suggested that a malignant mole showed significantly less depolarization than normal tissues and Lupus showed significant retardance. Liu *et al*. (2002) found that the decomposed images revealed more tissue structural information in rat skin and melanoma tissues. Chung *et al*. (2007) found that the decomposed depolarization and retardance images can be potentially useful in identifying precancerous lesions in oral tissue. Studies

on cervix tissues (Shukla, *et al*., 2008) also showed a significant difference in the diattenuation and depolarization parameters between normal and dysplasia tissues.

The details of the polar decomposition method and its application will be discussed in section 3.1.2.

1.3 Light Backscattering in Turbid Media

As most biological tissues have high scattering and low absorption, we need to thoroughly study light propagation in turbid media. For polarized light, the case is even more complicated. In scattering media, many changes in the polarization state of the propagating beam may happen, for example, the polarization of an initially unpolarized light or the depolarization of an initially polarized beam (Tuchin, *et al*., 2006).

Some biological tissues such as muscle or skin with fibrous structures have polarization anisotropy effect, which exhibits primarily as linear birefringence. The refractive index of the medium distributes differently along different orientation of the tissue (Tuchin, *et al*., 2006). So, polarized light propagating in a birefringent turbid media is rather more complicated.

We need to introduce the light backscattering in normal turbid media which may approximate or be compared to some biological tissues.

1.3.1 Scattering by Small Particles

Here, we use the turbid media with small particles as a tissue optical model. For this case, we need to apply the Mie theory to calculate the changes of light polarization in this medium. In 1908, a German physicist, Gustav Mie developed a theory to explain

light scattering and absorption by small colloidal particles of gold suspended in water. About the same time, Peter Debye first applied this theory to an astrophysical problem.

1.3.2 Single Scattering Approximation

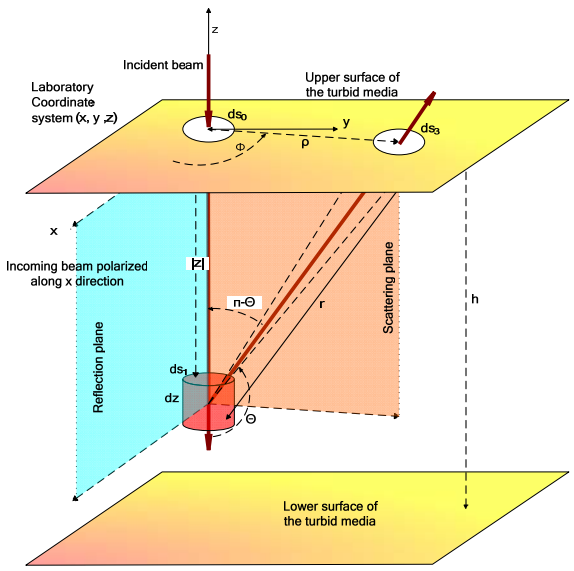

Fig. 1-2. Geometry for single scattering approximation (Wang, *et al*., 2002).

Fig. 1-2 shows the geometry for this single scattering approximation (Wang, *et al*., 2002). We assume that the backscattering light is reemitted mainly from the single-scattering events in the medium. The incoming narrow beam propagates down the z axis and is scattered back once in the lower half-space which is occupied with the scattering medium. The light exits the medium after one scattering and is detected by the detector. The interaction between the light and the medium surface is neglected. The thickness of the medium is h, and the scattering point is located in the lower half-space of the medium at z, $-h \le z \le 0$. A rotation matrix:

$$\mathbf{R}(\phi) = \begin{bmatrix} \cos\phi & \sin\phi \\ -\sin\phi & \cos\phi \end{bmatrix}, \tag{1-8}$$

transforms the Jones vector in the reference plane into one in the scattering plane. Another rotation matrix $R(-\phi)$ transforms the Jones vector of light back into the reference plane from the scattering plane when light exits the sample surface. The polarization state of any position can be described using the following equations:

$$\begin{bmatrix} E_x' \\ E_y' \end{bmatrix} = \begin{bmatrix} \cos\phi & -\sin\phi \\ \sin\phi & \cos\phi \end{bmatrix} \begin{bmatrix} S_2 & 0 \\ 0 & S_1 \end{bmatrix} \begin{bmatrix} \cos\phi & \sin\phi \\ -\sin\phi & \cos\phi \end{bmatrix} \begin{bmatrix} E_x \\ E_y \end{bmatrix}, \tag{1-9}$$

where φ is the angle between the laboratory and the reference coordinate systems. S_1 and S_2 could be calculated according to the Mie theory.

1.3.3 Double Scattering Approximation

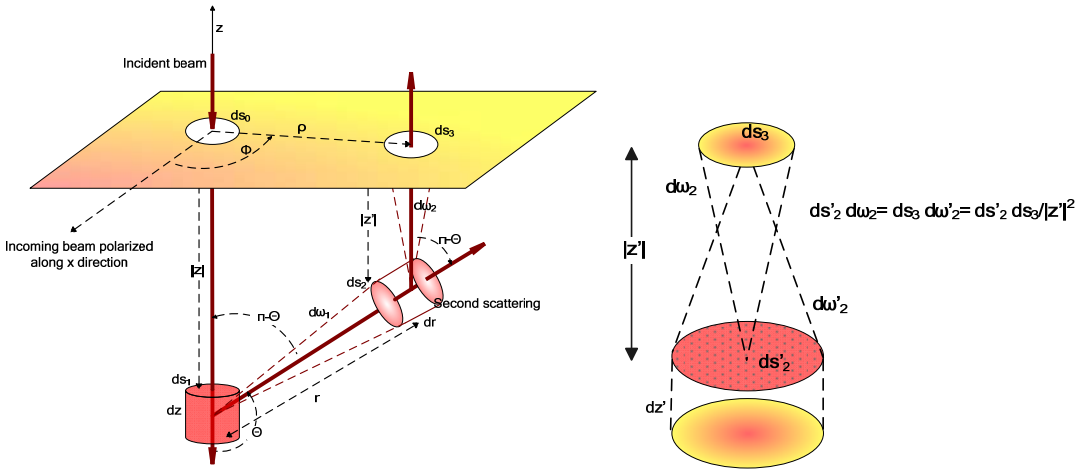

(a) (b)

Fig. 1-3. Geometry for double scattering approximation(Rakovic and Kattawar, 1998).

Fig. 1-3 shows the geometry for this double scattering approximation(Rakovic and Kattawar, 1998). We assume the backscattering patterns are produced when only the double scattering process is considered, and the light is scattered back parallel to the incident light. The incident light enters the medium downward along the z axis, and the first scattering occurs after propagating the length of $|z|$, $z \le 0$. The length from the first scattering point to the second scattering point is r, and the light will be scattered back upwards to the surface of the medium by propagating the length of $|z'|$, $z' \le 0$. The first scattering angle is θ, and the second scattering angle is $\pi - \theta$. ρ is the lateral distance from the laser input point to the scattering output point. The azimuth angle between the reference plane and the scattering plane is ϕ. We assume that the light crosses a small surface element ds_0 when propagating, and the total power of the light at the incident point is P_0. When it reaches the depth of $|z|$, the power is

$$\mathbf{P_1} = \mathbf{P_0}\, exp(-\mu_S |z|), \tag{1-10}$$

μ_T is the extinction coefficient. As in this ideal medium, the absorption is 0. So the extinction coefficient μ_T is equal to the scattering coefficient μ_S.

During the process of the first scattering, along with Eq. 1-2 (**M** is the 4×4 Mueller matrix which describes the single scattering process ,and $I_x + I_y = I_{+45^\circ} + I_{-45^\circ} = I_R + I_L$), the Stokes vector takes the form as follows (Bohren and Huffman, 1983):

$$\begin{bmatrix} S_0 \\ S_1 \\ S_2 \\ S_3 \end{bmatrix} = \begin{bmatrix} I_x + I_y \\ I_x - I_y \\ I_{+45^\circ} - I_{-45^\circ} \\ I_R - I_L \end{bmatrix} = \begin{bmatrix} I_x + I_y \\ I_x - I_y \\ 2I_{+45^\circ} - (I_x + I_y) \\ 2I_R - (I_x + I_y) \end{bmatrix}, \tag{1-11}$$

where I_x, I_y, I_{+45°, I_{-45°, I_R, I_L are the intensity of linear polarization along x direction (horizontal linear), linear polarization along y direction (vertical linear), linear polarization +45° to x direction ($+45^\circ$ linear), linear polarization -45° to x direction (-45° linear), right-handed circular, and left-handed circular polarization states, respectively.

Then the differential power:

$$d\mathbf{P}_2 = \mu_S dz \mathbf{M}(\theta)\mathbf{R}(-\phi)\mathbf{P}_1 d\omega_1 . \tag{1-12}$$

This function describes the differential power from the differential volume $dV_1 = ds_1 dz$ into the solid angle $d\omega_1$. And

$$\mathbf{R}(-\phi) = \begin{bmatrix} 1 & 0 & 0 & 0 \\ 0 & \cos 2\phi & \sin 2\phi & 0 \\ 0 & -\sin 2\phi & \cos 2\phi & 0 \\ 0 & 0 & 0 & 1 \end{bmatrix} \tag{1-13}$$

is the matrix that rotates the incident beam from the reference plane to the scattering plane. Here the angle looking in the direction of the initial beam is $-\phi$ because the direction of the rotation is counter-clockwise. $\mu_S dz$ describes the probability of the light scattering in infinitesimal distance dz. $d\omega_1 = ds_2 / r^2$ is the solid angle as seen from ds_1.

Subsequently, the light reaches the second scattering volume $dV_2 = ds_2 dr$ with the power of

$$d\mathbf{P_3} = d\mathbf{P_2}\, exp(-\mu_S r)\,. \tag{1-14}$$

After the process of the second scattering, the differential power that reaches the detector at ds_3 after rotating back to the reference plane can be described as:

$$d\mathbf{P_4} = \mu_S dr\, exp(-\mu_S |z'|)\mathbf{R}(\phi)\mathbf{M}(\pi-\theta)d\mathbf{P_3}d\omega_2\,. \tag{1-15}$$

Here $d\omega_2 = ds_3/|z'|^2$ is the solid angle as seen from ds_2.

Hence

$$d\mathbf{P_4} = \mu_S{}^2\, exp\left[-\mu_S\left(|z|+|z'|+r\right)\right]\mathbf{R}(\phi)\mathbf{M}(\pi-\theta)\mathbf{M}(\theta)\mathbf{R}(-\phi)\mathbf{P_0}d\omega_1 d\omega_2 dr dz\,. \tag{1-16}$$

The Stokes vector dI^{bs} describes the radiance at the detector so we need to divide the dP_4 by the area of ds_3 and the solid angle $d\omega_2'$ as in Fig. 1-3(b). (Referring to the definition of the radiance of any point of the detector (ds_3) from the source surface ds_2'). Here we assume $ds_2 dr = dV_2 = ds_2' dz'$, so we can treat the power in dV_2 as the light source, and ds_2' as the light source surface. As $d\omega_2 = ds_3/|z'|^2$ and $d\omega_2' = ds_2'/|z'|^2$, we have the relationship as: $ds_2' d\omega_2 = ds_3 d\omega_2' = ds_2' ds_3/|z'|^2$. Then we obtain:

$$d\mathbf{I}^{bs} = \frac{d\mathbf{P_4}}{ds_3 d\omega_2'} = \frac{d\mathbf{P_4}}{ds_2' d\omega_2} = \frac{d\mathbf{P_4}}{ds_2 dr d\omega_2}dz' = \frac{d\mathbf{P_4}}{d\omega_1 r^2 dr d\omega_2}dz' \tag{1-17}$$

Referring to Eq. 1-16,

$$d\mathbf{I}^{bs} = \mu_S{}^2\, exp\left[-\mu_S\left(|z|+|z'|+r\right)\right]\mathbf{R}(\phi)\mathbf{M}(\pi-\theta)\mathbf{M}(\theta)\mathbf{R}(-\phi)\mathbf{P_0}\frac{dzdz'}{r^2} \tag{1-18}$$

Rakovic and Kattawar (1998) successfully proved that if $\rho \to 0$, $\mathbf{P}^{bs}(\rho_0,\phi_0,\Delta s) \approx \mathbf{I}^{bs}(\rho_0,\phi_0)\Delta s$, then we have $\mathbf{P}_0 \approx \mathbf{I_0}$.

Above all, we get the equation to describe the intensity of the double scattering process of the surface of the medium:

$$\mathbf{I}^{\mathbf{bs}}(\rho,\phi) = {\mu_S}^2 \int_{-\infty}^{0}\int_{-\infty}^{0} \frac{dzdz'}{r^2} exp\left[-\mu_S\left(|z|+|z'|+r\right)\right]\mathbf{R}(\phi)\mathbf{M}(\pi-\theta)\mathbf{M}(\theta)\mathbf{R}(-\phi)\mathbf{I_0} \quad (1\text{-}19)$$

1.4 Light Transmission in Turbid Media

Light reflectance and transmittance imaging can help us understand light propagation in a slab biological tissue and phantoms (Jacques, *et al*., 1996; Roccoa, *et al*., 2008; Sankaran, *et al*., 2000, 2002). The intensity of transmittance light from tissue or another slab is very sensitive to the thickness, absorption and scattering coefficient of the media. Sankaran's study (Sankaran, *et al*., 2002) showed that two incident polarization states depolarized differently according to the different structure of the sample. In tissues modeled with diluted Mie scatterers, circularly polarized light is maintained better than linearly polarized light, however, in dense tissue, the situation is reversed.

1.5 Structures in Skeletal Muscle Tissue

Muscles are important for force generation and motion control in human and animals. Skeletal, cardiac and smooth muscle are three types of muscle, of which skeletal muscle takes up to 40%-50% body mass of an average adult male and 30%-40% of an average adult female. The main function of skeletal muscles is to support skeletal movement by contraction. In addition, skeletal muscles consume energy and take part in the metabolic process in animals and humans.

The structure of the skeletal muscle is very organized to fulfill its function. As well as cardiac muscle, skeletal muscle is striated muscle due to its subordinative structure. A single muscle contains hundreds of muscle fascicles, and each muscle fascicle is made up of a bundle of individual muscle fibers. The muscle fiber is a single muscle cell oriented in the longitudinal direction of the muscle. It contained bundles of filaments running along the axis of the cell which is called myofibrils (Berne and Levy, 1992).

Sarcomere is the basic contractile unit in myofibrils. It is oriented along the muscle fiber and can be observed by using light microscopy distinguishing the dark and light striations. The dark striation is termed A-band because it appears dark (anisotropic) under a microscope using polarized light, while the light striation is called I-band because it appears light (isotropic). The thick (myosin) and thin (actin) filament arrays form the contractile system: A-band contains the parallel-arranged thick filaments and I-band contains only thin filaments which anchors to the darkly staining structure termed the Z-line or Z-disk in the center of the I-band. The striation is repeating and the unit between one Z disks to the next is called one sarcomere. The thick filaments overlap the thin filaments within one sarcomere unit. H zone is the part of the A band where the thick and thin filaments do not overlap (Xia, 2007). In the center of the A-band lies the M line (Berne and Levy, 1992).

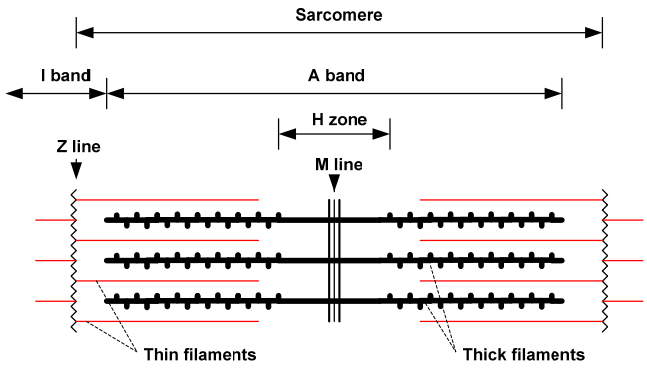

Fig. 1-4. Sketch map of sarcomere structure (Berne and Levy, 1992).

With the sliding filament model of muscle contraction, the thick and thin filaments slide past during the contraction and relaxation process. In the relaxed muscle, the thin (actin) and thick (myosin) filaments are aligned parallel to each other along the muscle fiber direction, and the H zones and I band have the maximum width at this moment. While contracting, the thin and thick filaments interact with each other. The thin filaments are pulled towards the center of the thick filaments next to them, so that the length of sarcomere decreases. In a fully contracted state, the thick filaments overlap, the I bands are very narrow, the A band does not change, and we can not see the H zone any more. In the whole process, the length of the sarcomere will change without changing the length of the filaments (Laing and Nowak, 2005).

As sarcomere is the fundamental unit of the skeletal muscle, more than 20 kinds of diseases are related to the mutation of the protein in sarcomere (Laing and Nowak, 2005).

1.6 Light Interaction with Skeletal Muscle

Because of the features of the skeletal muscle fiber, it generates diffraction for the incident monochromatic light. As a single muscle fiber has the size of about 100 μm across its diameter, it can be considered as a thick grating to some extent. Y. Yeh *et al* (1980) analyzed the light diffraction by single skeletal muscle fibers, and explained that the formation of diffraction pattern from the muscle is caused by the structure of muscle fiber and multiple scattering. Several theories of light diffraction in striated muscle have been developed since then Sidick *et al* (1992) applied the two-coupled wave theory to describe light diffraction by single muscle fiber, and they found that the diffraction efficiency is very sensitive to the difference in the sarcomere structure.

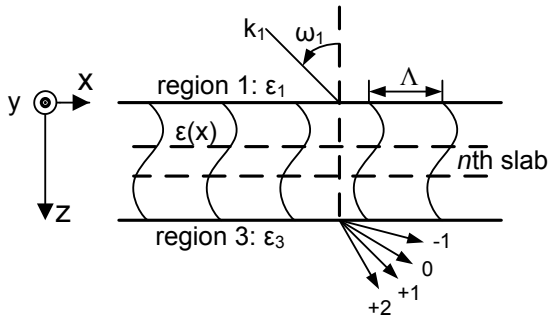

Fig. 1-5. Sketch map of two dimension single fiber diffraction (Sidick, *et al*., 1992).

As the structure of the skeletal muscle is distinctive, it showed the anisotropic optical properties. Zijp and ten Bosch (1998) measured the optical properties of bovine muscle tissue using different methods according to the angular intensity functions and spectral reflectance measurements. They also found a change of the optical properties between fresh muscle and frozen muscle. The anisotropy properties in chicken breast tissue, with respect to the absorption and scattering spectra, were also examined by

Marquez *et al*.(1998). Xia *et al* (2006) monitored the sarcomere structure changes in whole muscle by measuring the reduced scattering coefficient. They concluded that there is a strong correlation between the optical scattering properties and sarcomere length. This relationship can help to characterize the sarcomere structure changes *in vivo*.

1.7 Application of Polarized Light in Biological Field

Polarized light propagating in scattering biological media has been a hot topic for decades. It has been widely used in the biological field to detect particle numbers, particle sizes, axial ratios, size distributions and so on. Wyatt and Phillips (1972) used the scattering light to measure the radius of single airborne bacteria, and detected the lack of spherical symmetry of bacteria cell by depolarization. Bickel *et al*. (1976) applied scattering light to the bacterial spores, showing that certain elements or combinations of the elements in scattering matrix are sensitive to tiny structures in the particles. Backman *et al*. (1999) developed a polarized light scattering spectroscopy to analyze the histological information about the epithelial cells such as the size distribution of the cell nuclei and their refractive index. Itoh *et al*. (2005) analyzed the Mueller matrix of normal and spiny red blood cell suspensions, and found that fine structures on the human blood cells will cause differences in the DOP of circular polarized light.

When propagating in turbid media, a polarized light may retain some of the polarization information. A study also demonstrated that the depolarization of light propagating in tissue depends on the wavelength of the light and the type of tissue it propagates. So this can be used to improve optical mammography for tumors (Demos*, et al.*, 1996). Demos and Alfano (1997) developed a system to take polarized images from

the retroreflection geometry to view the surface as well as the structure beneath the surface. It was demonstrated that the images of structures at different depths can be obtained by the use of a perpendicular polarization component (images taken while the axis of the polarizer is perpendicular to that of the analyzer) and different wavelength of the light. Jacques *et al* (2000; 2002; 1996) did a lot of work applying this technique to study skin pathology and to detect skin cancer.

CHAPTER 2

POLARIZED REFLECTANCE IMAGING

2.1 Materials and Methods

To record the reflectance polarization images of muscles or other highly scattering medium, a setup should be well designed. The distance from the lens to the sample should be adjusted according to the image recording device (such as CCD). Before the experiment, the laser beam should be aligned and the whole setup should be carefully calibrated.

2.1.1 Experimental Setup

Our experimental setup is shown in Fig. 2-1. The beam from a 632.8 nm linearly polarized He-Ne laser was oriented into the system. The Half waveplate #1 can rotate the polarization direction from the light source, and Mirror #1 will change the beam direction perpendicular to the platform. Linear polarizer #1 will purify the polarized light more, and the variable waveplate can be adjusted to produce any linear or circular polarization state. The incident light passes through a 1.0 mm hole of a mirror arranged at 45^{o} to reflect the backscattered image through the quarter waveplate and linear polarizer #2 towards the CCD camera. The CCD used was an 8-bit video camera with a 50mm f/2.8 imaging lens. A fixed aperture of f/8 was used throughout the experiments. The entire

system was carefully aligned to ensure polarization extinction ratios of <-40.6dB and <-31.7dB for linearly and circularly polarized light, respectively. The camera aperture accepted photons within 1.2° of normal over a 26.5×19.9mm^2 (Fig. 2-3) imaging area which stands for 640*480 pixels.

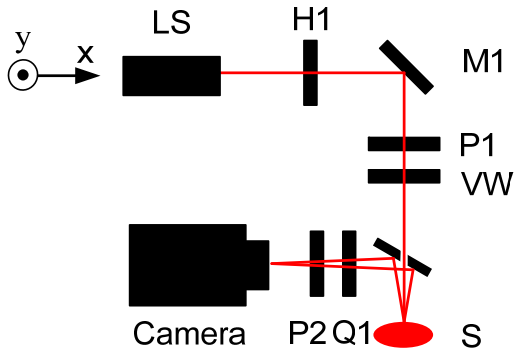

Fig. 2-1. Schematic of experimental setup: LS: a 10mW He-Ne laser; H1: half wave plate; M1: mirror; P1: polarizer; VW: variable waveplate; M2: mirror; S: sample; Q1: quarter waveplate; P2: polarizer; CCD: imaging camera.

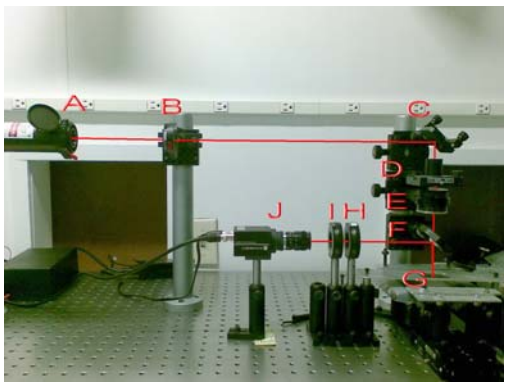

Fig. 2-2 Photo of actual experimental setup.

Table 2-1. The setup components

Tab	Component	Remarks
A	Laser	623.8 nm He-Ne laser
B	Half waveplate #1	THORLABS WPH05M-633
C	Mirror #1	
D	Linear polarizer #1	
E	Variable waveplate	New. Focus Model 5540
F	Mirror #2 (45^o)	With a 1mm hole 45^o in the center
G	Target location	
H	Quarter waveplate	THORLABS WPQ05M-633
I	Linear polarizer #2	THORLABS LPVISB100
J	CCD camera	Allen Bradley 2801 YF, 640×480

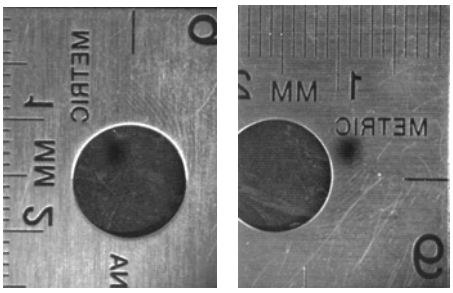

Fig. 2-3. Size of recorded images.

A Labview program was compiled to control the process of acquiring images continuously with adjustable intervals between two acquisitions. This program can also average these images, and normalize them by the incident intensity as a final result image. Other Labview programs (or Matlab programs) were as well written to calculate the Mueller matrix images, DOP images, and so on.

2.1.2 Calibration Process

a. Beam Alignment

We need to make sure the beam from the laser is parallel to the table axis by moving an iris with fixed height. After being reflected by mirror #1, the beam can be

oriented to a liquid surface, superposition of the reflected beam spot and the original beam spot will guarantee the beam is perpendicular to the horizontal surface. The aligned beam should pass through the center of the each lens and through mirror #2 with a hole at 45^{o}. The beam spot after passing through the hole should have no pattern and remain with as much intensity as possible. To make sure mirror #2 is 45^{o}, light should also be directed to a liquid surface, and use a pinhole to check if the reflected light pattern is at the same height.

b. Define Laboratorial Direction

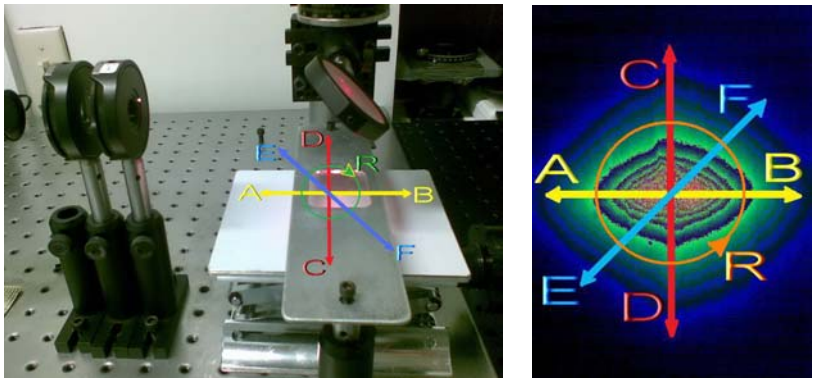

(a) (b)

Fig. 2-4. Directions defined in the system and recorded images. A reference coordinate system is defined in Fig. 2-4(a), and the direction corresponding to that of the system in the recorded images is shown in Fig. 2-4(b).

The incident light propagates perpendicular to the experimental table (horizontal plane). It should be noticed that all the directions are defined when the incident is toward the viewer. The H incident is along the yellow arrow (the A-B direction), the V incident is along red arrow (the C-D direction), and the P ($+45^{o}$) incident is along the blue arrow (the E-F direction). M (-45^{o}) incident direction is perpendicular to P. R in the above figures describes direction of the right-handed circular polarized light. L (left-handed

circular polarized light) is just opposite of R. The muscle is put perpendicular to the H incident along the red arrow (C-D direction).

c. Calibration of Input Branch

The whole elements in the system were calibrated by a nulling technique using a polarizer and quarter waveplate. Each component of the system will be adjusted to a different state and will be calibrated by detecting the minimum power value from the power detector (Newport Optical Metter 1830-C).

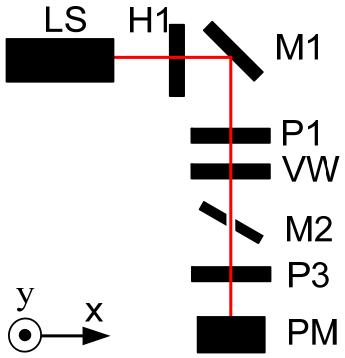

Fig. 2-5. Schematic of input calibration.

To calibrate the input branch, we added a polarizer P3 under Mirror #2, perpendicular to the incident light, and let the incident pass through the center of the plate. The power meter PM should be placed under P3. H1 was used to adjust the total intensity of the incident, and the light axis of P1 was placed in the V direction.

For the H, V, P and R input state, place the axis of P3 perpendicular to the corresponding direction, and adjust the retarder and rotator of VW till the power meter gets the minimum value. For R (L) input state, a quarter waveplate Q3 with its axis along

V (H) direction should be placed between VW and P3. The axis of P3 should be placed in the M direction, and VW should be adjusted till the power meter gets minimum value.

d. Calibration of Output Branch

To calibrate the output branch for the system, we needed to remove P3, Q3 and the power meter, and add a reflection mirror #3 under M2. M3 should be nearly 90 degrees to the incident light, so that the reflected light to M2 could avoid the hole and be directed to the output branch. The power meter should be put after P2.

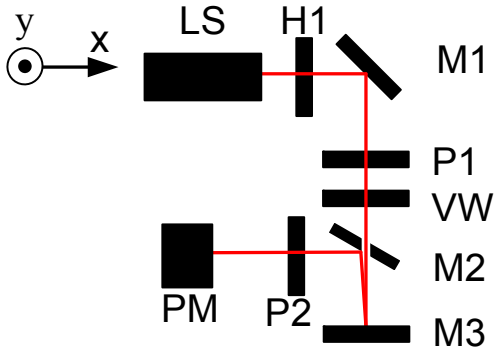

Fig. 2-6. Schematic of output calibration.

For the output state (such as H, V, P, and R), the opposite input state (such as V, H, M, and L) should be adjusted first, Q1 and P2 should then be adjusted till the power meter reaches the minimum value.

2.1.3 Specimens

a. Muscle Strip

The muscle we used was Bovine *Sternomandibularis* excised from the animal right after slaughtering at the Meat Science Laboratory in the University of Missouri. The

fat tissues should be removed and the connective tissue—epimysium should remain in order to protect the muscle bundles. The longitude of the muscle should be placed along CD direction in Fig. 2-4 which is the direction of vertical polarization, so that the muscle fiber is oriented along the direction of vertical polarization. Both ends of the muscle should be fixed to the sample holder by adhesive tape tightly against the muscle contraction. A thin cover glass will be applied on the muscle to insure the imaging surface is even. To avoid an intensive reflection spot from the cover glass, it needs to be tilted into a small angle about 7^{o}. At the bottom of the specimen, a black paper should be applied to eliminate the interference from the sample holder.

b. Polystyrene Solution

The polystyrene (1.093 μm in diameter) is diluted with distilled water, and mixed well. The concentration of the solution should be recorded and adjusted for a different use of the experiment. While taking images, the container should by slightly shacked in order to give smooth images.

2.2 Results and Discussion

2.2.1 Polarization Imaging Result

In our measurements, three different linearly polarized states were used: H, V, P, whose polarization directions were aligned with the x-axis, y-axis, and 45^{o} to x-axis, respectively. In addition, the right-handed circularly polarized state R was also used. Fig. 2-7 shows the reflectance polarization images of 0.12% concentration polystyrene solution with 16 different combinations of incident and detection polarization states. Each

image is the average of 40 images with the interval of 20 ms. The incident point is at the center. To better illustrate the relationship between the muscle orientation and intensity decay, the images are shown in a pseudo-color depiction of the equi-intensity distribution. In other words, the same color in the image represents all pixels of the same intensity.

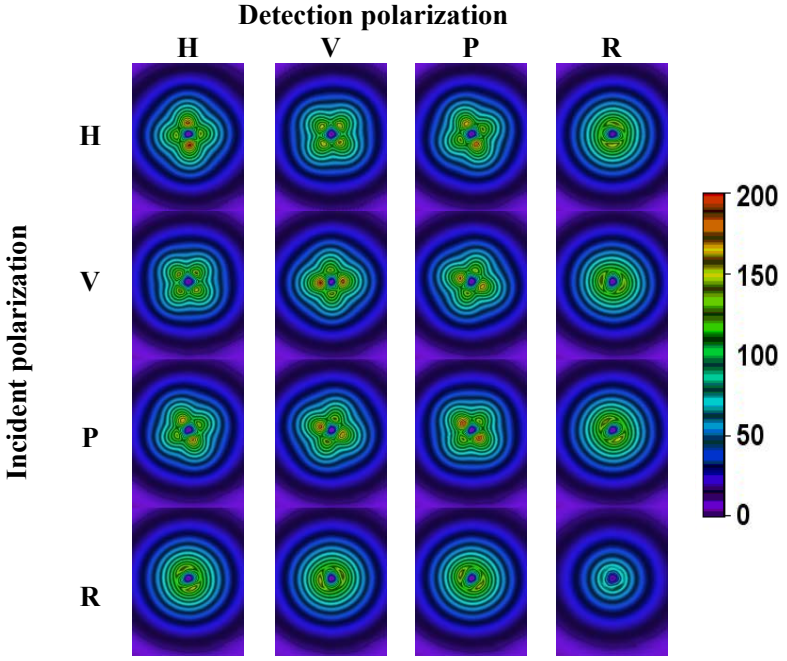

Fig. 2-7. Polarization-sensitive reflectance images in 2.62% polystyrene solution with 0.12% concentration. The diameter of the polystyrene particles is 1.093 μ m, and the thickness of the solution is 35mm. The optical parameter of the solution is μ_a =0, μ_s =44cm^{-1}, g=0.93, μ_s' =3.26cm^{-1}. The image size was 24.5mm by 18.4mm. The H-polarization direction was along the x-axis.

From the 16 combinations of the polarization states, a diagonal symmetric relationship between incident polarization and detection polarization can be identified from the images. For example, HV and VH are almost identical to each other. So we just need to describe part of these images such as HH, VH, VV, PH, PV, PP, RH, RV, RP and RR. For RH, RV and RP, the ellipse shapes appear within a small distance to the incident

point and the circular shapes appear within a large distance to the incident point. A set of circular shapes with the same center appear in RR and the signal is very weak compared to others. The long axis of the ellipse in RH is along y-axis, in RV it is along the x-axis and in RP it is along -45^{o} to x-axis. Other images that need to be described have a cross shape with a small distance to the incident point and have a rhombus-like shape with a large distance to the incident point. For VH, the cross shape is almost radially symmetrical, and others have one contrapuntal pair larger than the other. HH, VV and PP have larger intensity on the large contrapuntal pair with a certain distance to the incident point than other images. The long axes of the large contrapuntal pairs are along y-axis, x-axis and -45^{o} to x-axis.

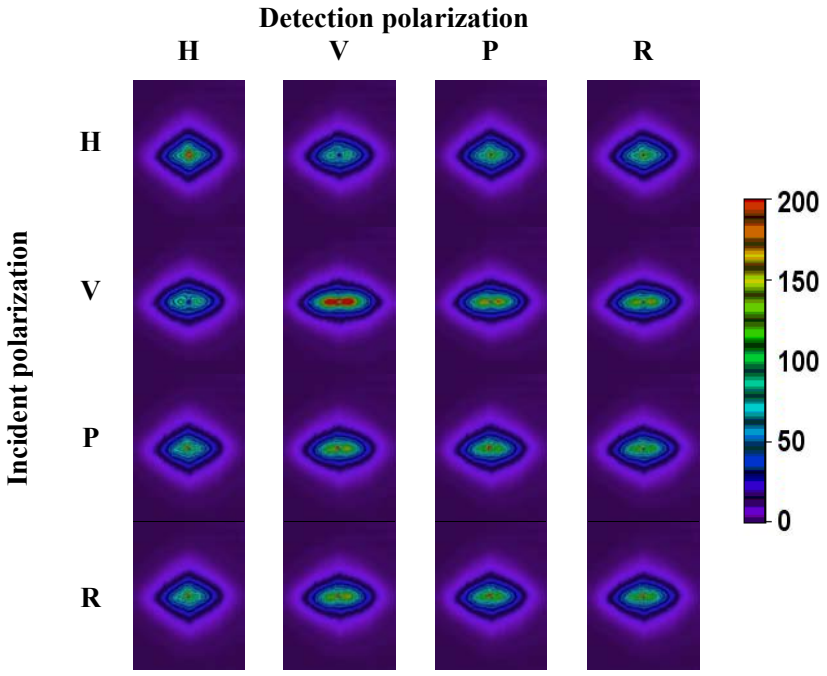

Fig. 2-8. Polarization-sensitive reflectance images in skeletal muscle. The incident light was located at the center of the image. The image size was 26.5 mm by 19.9 mm. The muscle fibers were along the vertical direction (y-axis). The H-polarization direction was along the horizontal direction.

Fig. 2-8 shows the reflectance polarization images of a muscle sample acquired with 16 different combinations of incident and detection polarization states. Each image is the average of 40 images with the interval of 400ms. The incident point is at the center, and the muscle was mounted such that the muscle fiber was oriented along the vertical direction (y-axis) of the image. To better illustrate the relationship between the muscle orientation and intensity decay, the images are shown in a pseudo-color depiction of the equi-intensity distribution. In other words, the same color in the image represents all pixels of the same intensity.

Fig. 2-8 shows that the equi-intensity profiles of all the acquired images appear to have a rhombus shape, similar to what was observed in our previous non-polarized imaging study (Ranasinghesagara and Yao, 2007). Differences exist, however, among images acquired with different polarizations. The most significant difference is found between the HH and VV images. The VV image has the strongest signal among all the images, and its inner equi-intensity profile is elongated along the horizontal direction. The HH image shows very strong rhombus profiles. The equi-intensity profiles of other images have patterns that lie in between those of the HH and VV images. A diagonal symmetric relationship between incident polarization and detection polarization can be identified from the images. For example, HV and VH are very similar to each other.

2.2.2 Levenberg-Marquet Fitting Results

Similar to the reflectance image obtained with unpolarized light, the polarization-sensitive images shown in Fig. 2-8 can be fitted using the following equation (Ranasinghesagara and Yao, 2007):

$$f(x,y)=\left(\frac{|x|}{a}\right)^{q}+\left(\frac{|y|}{b}\right)^{q}-1=0\,. \qquad (2\text{-}1)$$

The patterns described by the above equation transition from a rhombus to an ellipse as the parameter q increases from 1 to 2. The parameters a and b indicate the axis length along the x and y-axis, respectively. The three parameters a, b, and q can be estimated by using the Levenberg-Marquet (LM) nonlinear fitting algorithm (Press, *et al*., 1992).

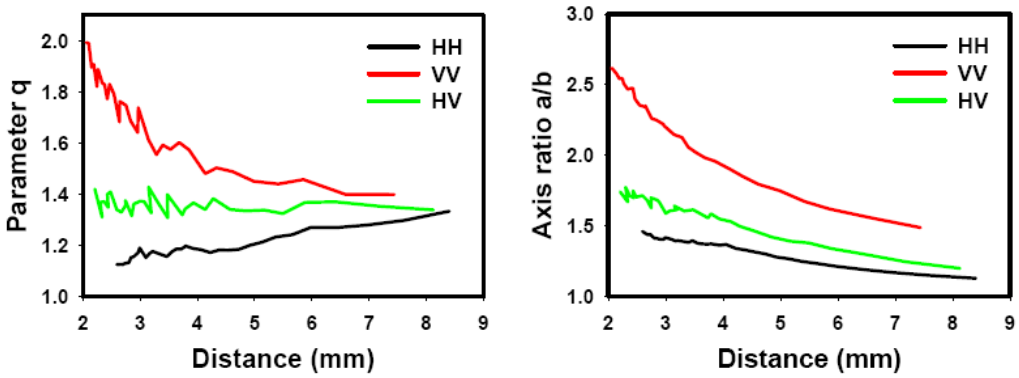

Fig. 2-9. Fitting results of the parameter q and the axis ratio (a/b) for the HH, HV, VV images shown in Fig. 2-8 obtained at different distances along the y-axis from the incident point.

From the numerical fitting results shown in Fig. 2-9, the equi-intensity patterns obtained in HH, HV, and VV images are indeed found to be different. At small distances from the incident point, the HH image is almost an exact rhombus with a q value approaching 1.0. In contrast, the VV image has an exact elliptical pattern with a q value of 2.0. The HV images have a pattern between a rhombus and an ellipse. As the distance from the incident point increases, the q-value in the HH image increases while the q-value in the VV image decreases. The q-value in the HV image remains quite stable at the entire 2-8 mm distance from the incident point. At larger distances, the fitted q-values

in all HH, HV, and VV images converge to a value of ~1.4, which is similar to the value obtained in an unpolarized reflectance image (Ranasinghesagara and Yao, 2007). The ratio of the two axes in all three images decreases with the distance. The decrease in VV, from >2.5 at 2 mm to ~1.5 at 8 mm, is the most significant. The trend implies that the anisotropic effect was reduced at larger distances because of multiple scattering.

2.2.3 Stokes Vectors

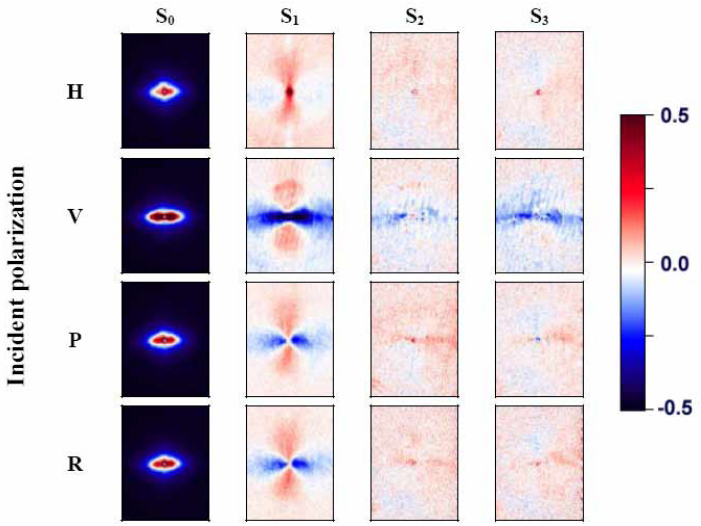

Fig. 2-10. Stokes vectors of the reflectance images in a muscle for 4 different incident polarization states: H, V, P and R. The images were calculated from the raw images in Fig. 2-8 using Eq.1-2. The S_1, S_2, and S_3 images were normalized with the S_0 image. The color map shown was used for S_1, S_2, and S_3 images only. The muscle fibers were along the vertical direction. The H-polarization direction was along the horizontal direction.

Fig. 2-10 shows the calculated Stokes vectors of the reflectance image at the four different incident polarization states H, V, P, and R. As can be seen, the second Stokes component S_1 show the same "cross-like" patterns for all four incident polarization states, although their intensity distributions are quite different. Because the S_1 Stokes component

represents the difference in the H and V polarization components of the back-reflected light, the results indicate that the reflected light has a larger H-polarized component along the y-axis or the muscle fiber orientation and a larger V-polarized component perpendicular to the muscle fibers. Their relative weights, however, are significantly different. In the S_1 component of the Stokes vector obtained with H incidence, the V component along the x-axis is barely larger than the H component while in the case of V incidence, the V component is clearly dominant. The Stokes vectors obtained with P and R incident light are almost the same. There are no significant patterns in the S_2 and S_3 Stokes components obtained for all four different incident polarization states. It is interesting to note that, with circularly polarized incident light, the reflectance Stokes vector has a strong pattern in the S_1 component and a plain S_3 component. This implies that the incident circularly polarized light is converted into linearly polarized light, likely resulting from muscle birefringence (Pasquesi, *et al.*, 2006).

2.2.4 Mueller Matrix Images

The Mueller matrix images (Fig. 2-11) of the muscle sample were calculated using Eq. 1-3. As a comparison, the Mueller matrices obtained in a polystyrene (Polysciences, Inc., Warrington, PA) solution are also shown. The diameter of the polystyrene sphere was 1.093 μm. A volume concentration of 0.12% was used in the study with a calculated scattering coefficient of 44 cm^{-1} and anisotropy of 0.93. The Mueller matrix images obtained in the polystyrene solution are similar to those reported before (Deng*, et al.*, 2007; Hielscher*, et al.*, 1997; Schwartz and Dogariu, 2008; Yao and Wang, 2000). The M11 component of the Mueller matrix represents the unpolarized

measurements. As expected, the equi-intensity profiles of the M11 element in polystyrene solution are a set of circles centered at the incident point with the reflectance intensity decreasing with the radial distance. In contrast, the M11 component in muscle has the typical rhombus profile as discussed before.

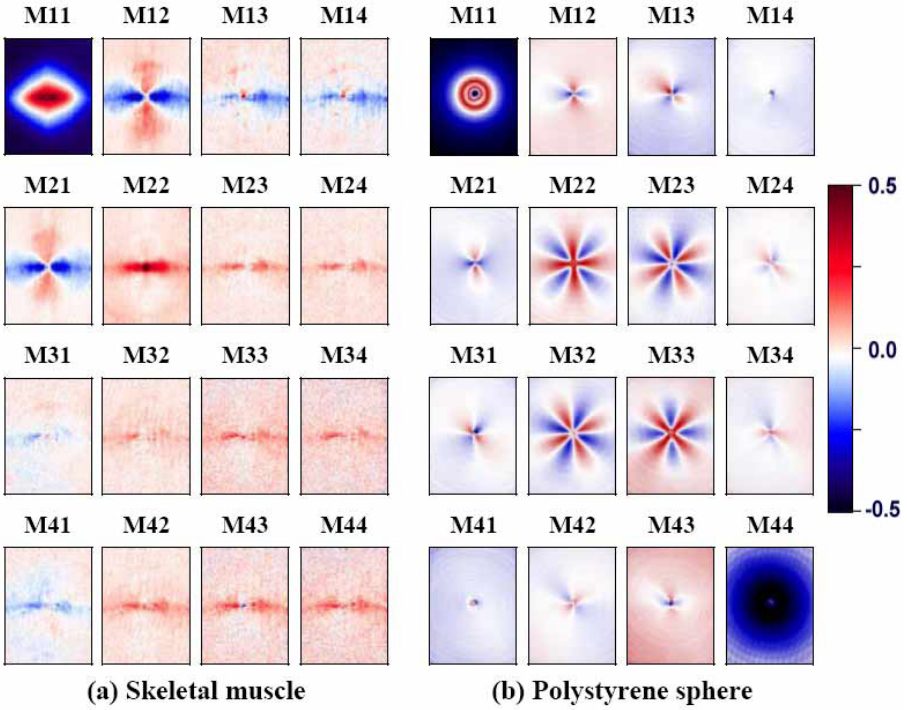

Fig. 2-11. Mueller matrices of the reflectance images in a muscle sample. The images were calculated from the raw images in Fig. 2-8 by using Eq. 1-3. The muscle fibers were along vertical direction. The H-polarization direction was along the horizontal direction. All images were normalized with the M11 image. As a comparison, the Mueller matrices obtained in a polystyrene (1.093 μ m in diameter) solution were also shown. Please note that the M11 images used in their own color maps.

The equi-intensity profiles of the M12 and M21 elements in both muscle and polystyrene solution have similar shapes of quatrefoils. The intensity values along the x-axis are negative, and those along the y-axis are positive. A close examination indicates

that the intensity distributions along the x- and y-axis are similar in polystyrene solution, while the signal along the x-axis is ~3 times larger than that along the y-axis in muscle. Similarly, in polystyrene solution, the M22 has a symmetric cross-like pattern with an almost identical intensity distribution along the x- and y-axis. In skeletal muscle, however, the M22 pattern along the muscle fiber orientation (the y-axis) is very weak, while the signal along the x-axis is dominant. The other symbolic patterns shown in M23, M32, M33, and M44 from polystyrene solution do not present in the images obtained in muscle. Instead there appear to be some residual patterns along the x-axis in the muscle images.

In an isotropic medium (such as polystyrene solution), the patterns of the polarization-sensitive reflectance image can be described by the single-scattering approximation as discussed before (Wang, *et al*., 2002). For example, the typical quatrefoils patterns shown in the M12 and M21 images can be predicted by using the standard Mie scattering matrix. The appearance of such patterns in the muscle sample suggests that the Mie scattering mechanism still operates in this complex tissue.

2.2.5 Double-Scattering Approximation

Using the theories in section 1.3.3, we can approximate the polarization reflectance images of isotropic solution with the Mie theory. Here we calculated some elements of reflectance polarization images and the Mueller matrix.

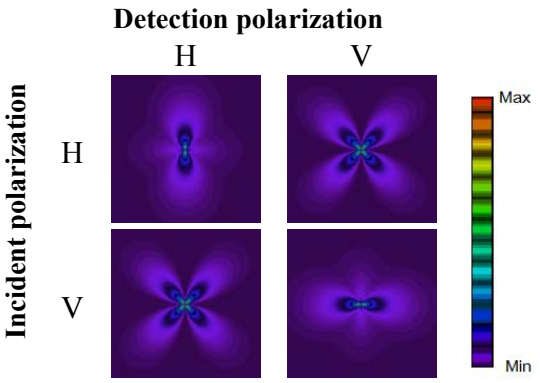

Fig. 2-12. Calculated Polarization-sensitive reflectance images of HH, HV, VH and VV in 0.12% concentration polystyrene solution. The diameter of the polystyrene particles is 1.093 μm, the optical parameter of the solution is μ_a=0, μ_s=44 cm^{-1}, g=0.93, μ_s'=3 cm^{-1}. The 0^o directions of ϕ in these images are all along x axis.

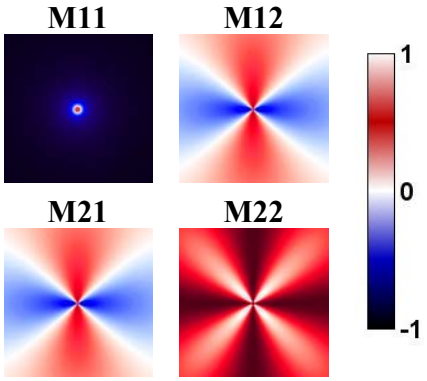

Fig. 2-13. Calculated Mueller matrix elements of M11, M12, M21 and M22 in 0.12% concentration polystyrene solution. All images were normalized with the M11 image. Please note that the M11 images used in their own color maps.

Fig. 2-13 shows that the approximation of the reflectance polarization images show similar shapes as those patterns with a small distance from the incident point of the experimental images. However, the profiles with a large distance from the incident point in the experimental images could not be shown. For the 4 Mueller matrix elements of M11, M12, M21 and M22, the patterns in the approximation images are similar to the experimental results.

In that case, we can see that the double scattering theory can approximate the polarization imaging on isotropic solution to some extent. However, it is still limited.

2.2.6 DOP Images

All our imaging results, however, identify a clear preference along the x-axis, the direction perpendicular to the muscle fibers. To obtain further insight into such anisotropic effect, we calculated degree-of-polarization (DOP) images for the 4 different incident polarization states H, V, P, and R.

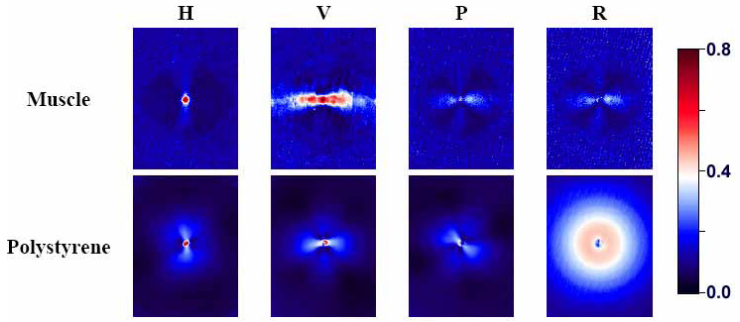

Fig. 2-14. Images of the degree of polarization (DOP) calculated from the Stokes vector images in Fig. 2-10 by using Eq. 1-7. The muscle fibers were along the vertical direction. The H-polarization direction was along the horizontal direction. As a comparison, the DOP images obtained in a polystyrene solution were also shown.

As shown in Fig. 2-14, the DOP images from the muscle sample and the polystyrene solution are significantly different. With linearly polarized incident light, the reflected light in the polystyrene solution maintains a certain polarization along the direction orthogonal to the original polarization direction. For example, the incident H polarization is aligned with the x axis in Fig. 2-14, while the corresponding reflected light has a high degree of polarization along the y-axis within a small area. Due to the

polarization memory effects (Nothdurft and Yao, 2006), a circularly polarized incident light produces polarization-preserving backscattered light over a large area.

In muscle, the x-axis preference appears again in the DOP images. With V-polarized incident light, the back-reflected light preserves polarization over a much longer distance along the x axis: the DOP is close to 0.5 even at 5 mm distance from the incident location. The polarization memory effect disappears in muscle with circularly polarized incident light. Even with P- and R-polarized incident light, the backscattered photons maintain a higher polarization at locations along the x-axis.

It is known that multiple scattering depolarizes incident polarized light, especially linearly polarized light. Therefore the DOP of the backscattered light can be used as an indicator of the number of scatterings. At a larger distance from the incidence, the DOP is generally close to zero in both samples due to multiple scatterings. Those photons exiting at a smaller distance from the incidence experience fewer scatterings and thus maintain certain polarization. The orientation of DOP patterns in the polystyrene sample can be explained by using a single Mie scattering theory (Wang, *et al*., 2002). For example, a Mie particle tends to scatter more polarization maintained V-polarized incident light in the orthogonal direction (x-axis in Fig. 2-14). In muscle, such tendency is greatly enhanced for the V-polarized incident light, which indicates a much smaller scattering probability along the x-axis for this particular polarization. In other words, V-polarized incident photons experience a longer pathlength along the y-axis and are subject to more attenuations, which is supported by the greater than 1.0 axis ratio of a/b as shown in Fig. 2-9. In addition, the backscattered light along the x-axis is primarily V polarized as shown in Fig. 2-10.

This phenomenon is most likely caused by the diffraction effect of the unique muscle sarcomere structures. To provide some quantitative evidence, we calculated the diffraction efficiencies of the muscle fiber when light is scattered back to the surface within a plane perpendicular to muscle fibers, i.e., along the x-axis (Fig. 2-15), by using a three dimensional coupled wave theory (Moharam and Gaylord, 1983; Ranasinghesagara and Yao, 2007). A physical sarcomere structure model and properties proposed by Thornhill *et al*. (1991) was used in the calculation (Ranasinghesagara and Yao, 2007). The sarcomere length used was 2.8 μm. Other sarcomere lengths led to the same conclusion. As shown in Fig. 2-15, the periodic sarcomere structure clearly diffracts much less V-polarized (TE polarization) light away than H-polarized light (TM polarization). Therefore, most of the light reaching back to the surface along the x-axis is V-polarized as observed in this study.

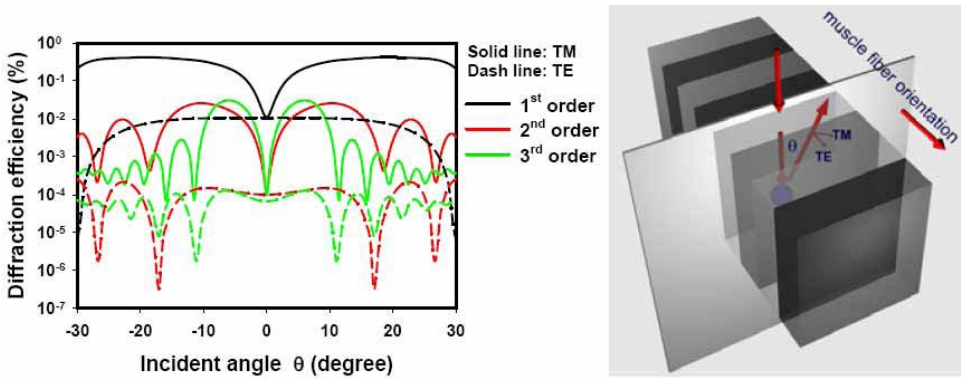

Fig. 2-15. Diffraction efficiencies for the first 3 diffraction orders calculated by using coupled wave theory. The curves shown in solid lines are for TM polarization component, while those shown in dash lines are for TE polarization components. The geometry of the calculation is also illustrated in the figure. Please note that the TE direction is aligned with the muscle fiber orientation (y-axis) and the V-polarization in our coordinate system.

2.3 Conclusion

We acquired polarization-sensitive reflectance images in fresh bovine *sternomandibularis* muscle. The whole Mueller matrix images were computed and compared with those obtained in a well-studied polystyrene solution. A double scattering simulation results were also shown. Our experimental results indicate that the propagation of polarized light in muscle is significantly different from that in media of spherical particles. Although more quantitative studies are needed, experimental evidence indicates that the scattering by spherical particles, muscle-fiber-induced birefringence, and sarcomere-induced diffraction may all contribute to the results observed in this study. The most important difference between striated muscle and other biological tissue is the periodic sarcomere structures. Their strong effects must be taken into consideration when applying optical measurements to muscle tissues. In addition, because sarcomere is a critical component for normal muscle functions as well as meat quality, its distinct effect on light transport should be explored to develop optical techniques that can assess its structural and functional properties noninvasively.

CHAPTER 3

POLAR DECOMPOSITION OF REFLECTANCE IMAGING IN STRETCHED SKELETAL MUSCLE

3.1 Materials and Methods

3.1.1 Experimental Setup

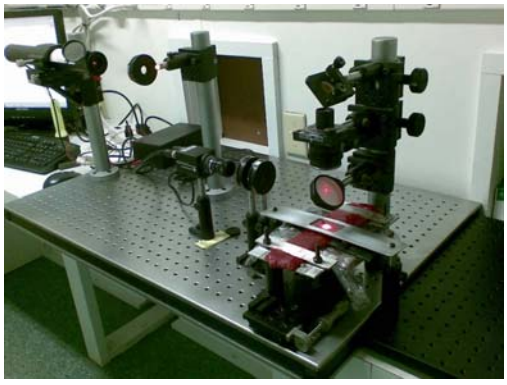

Fig. 3-1. Photo of actual experimental setup.

The experimental setup (Fig. 3-1) is almost the same with the setup in Chapter 2 (Fig. 2-1). The only difference is that the sample holder is replaced by a sliding stage which can slide along a vertical direction (CD direction in Fig. 2-4) which is able to stretch the muscle for a certain length. One clamp should be fixed on the sliding stage, and the other clamp should be fixed on the table. During the experiment, the muscle strip will be fixed at the two clamps on the end. The top of the sample holder should be blacked out and covered with plastic paper to supply a slippery surface. A cover glass

should also be applied to the sample surface as before. The distance between the two clamps is 11cm before stretching.

Bovine *sternomandibularis* muscles were excised from animals immediately after slaughtering. After removing fat tissues, the sample was mounted on the sample holder with both ends fixed to ensure a constant sample length. A cover glass was applied on the sample surface to ensure a flat imaging surface. The muscle sample in its natural state had a width of ~ 6 cm and a thickness of ~1.2 cm. The original length of the muscle was 11 cm between the two mounted ends. For the stretching test, the sample was stretched 20% of its original length along the muscle fibers.

The full Mueller matrices were calculated from a total of 16 polarization reflectance images recorded from sample using the same method described before in the previous chapter (section 2.2.3). Thus a total of 16 images were acquired with the combination of the aforementioned four different input states (realized by the variable waveplate VW) and four different output states (realized by the combination of P2 and Q). Each image was averaged by 40 times to reduce noise. The Muller matrix was calculated from these raw images:

$$\boldsymbol{M} = \begin{bmatrix} m_{11} & m_{12} & m_{13} & m_{14} \\ m_{21} & m_{22} & m_{23} & m_{24} \\ m_{31} & m_{32} & m_{33} & m_{34} \\ m_{41} & m_{42} & m_{43} & m_{44} \end{bmatrix} \quad , \quad (3\text{-}1)$$

$$= \begin{bmatrix} HH+HV+VH+VV & HH+HV-VH-VV & 2PH+2PV-m_{11} & 2RH+2RV-m_{11} \\ HH-HV+VH-VV & HH-HV-VH+VV & 2PH-2PV-m_{21} & 2RH-2RV-m_{21} \\ 2HP+2VP-m_{11} & 2HP-2VP-m_{12} & 4PP-2PH-2PV-m_{31} & 4RP-2RH-2RV-m_{31} \\ 2HR+2VR-m_{11} & 2HR-2VR-m_{12} & 4PR-2PH-2PV-m_{41} & 4RR-2RH-2RV-m_{41} \end{bmatrix}$$

where each measure is represented by two letters. The first letter denotes the input polarization state and the second letter denotes the measurement polarization state. For

example, HV represents an image acquired when the incident polarization is H and detection polarization is V. All elements are normalized against the first element m_{11}.

3.1.2 Polar Decomposition

Polar decomposition algorithm is used to extract several polarization parameters from the whole Mueller matrix. Theoretically, there are multiple possible decomposition families (Ossikovski, *et al*., 2007). In this study, we applied the original method introduced by Lu and Chipman (1996) and used by others (Ghosh and Wood, 2008; Manhas, *et al*., 2006; Swami, *et al*., 2006) for tissue characterizations. A brief description of the procedures applied in this study is given below.

The 4×4 Mueller matrix is decomposed as the product of three matrices corresponding to a depolarizer ($\mathbf{M}_\Delta$), a retarder ($\mathbf{M}_\mathrm{R}$), and a diattenuator ($\mathbf{M}_\mathrm{D}$):

$$\mathbf{M} = \mathbf{M}_\Delta \mathbf{M}_R \mathbf{M}_D . \tag{3-2}$$

With the depolarization matrix in front of the diattenuation matrix, such decomposition always produces physically possible Mueller matrices (Mario and Goudail, 2004). The corresponding three individual Mueller matrices have the following standard forms:

$$\begin{aligned} \boldsymbol{M}_\Delta &= \begin{bmatrix} 1 & \vec{0}^T \\ \vec{P}_\Delta & \boldsymbol{m}_\Delta \end{bmatrix} \\ \boldsymbol{M}_R &= \begin{bmatrix} 1 & \vec{0}^T \\ \vec{0} & \boldsymbol{m}_R \end{bmatrix} , \\ \boldsymbol{M}_D &= \begin{bmatrix} 1 & \vec{D}^T \\ \vec{D} & \boldsymbol{m}_D \end{bmatrix} \end{aligned} \tag{3-3}$$

where the small case arrays **m** represent 3×3 submatrices. Specifically, the diattenuation submatrix $\mathbf{m}_\mathrm{D}$ can be written as:

$$\boldsymbol{m}_D = \sqrt{1-D^2}\,\boldsymbol{I} + \frac{1-\sqrt{1-D^2}}{D^2}\vec{D}\vec{D}^T, \tag{3-4}$$

where **I** is the 3×3 unity matrix; $\vec{D}$ is the diattenuation vector, and the diattenuation value D is the length of the diattenuation vector $D = \left|\vec{D}\right|$.

By multiplying the three standard matrices in Eq. 3-3, it is clear that the diattenuation vector can be directly derived from the measured Mueller matrix (normalized by m_{11} element):

$$\vec{D} = \begin{bmatrix} m_{12} & m_{13} & m_{14} \end{bmatrix}^T, \tag{3-5}$$

where m_{ij} is the ith row and jth column element of the Mueller matrix **M**. The diattenuation can be calculated as: $D = \sqrt{m_{12}^2 + m_{13}^2 + m_{14}^2}$.

The depolarization submatrix $\mathbf{m}_\Delta$ is a symmetric matrix whose eigenvectors describe its depolarization capabilities along the three orthogonal axes. And the $\vec{\mathbf{P}}_\Delta$ describes its polarizance. After obtaining $\mathbf{M}_D$ according to Eq. 3-4, the product of the depolarizing matrix ($\mathbf{M}_\Delta$) and the retardance matrix ($\mathbf{M}_R$) becomes:

$$\boldsymbol{M}_\Delta \boldsymbol{M}_R = \begin{bmatrix} 1 & \vec{0}^T \\ \vec{P}_\Delta & \boldsymbol{m}' \end{bmatrix} = \boldsymbol{M}\boldsymbol{M}_D^{-1}, \tag{3-6}$$

where $\mathbf{m}' = \mathbf{m}_\Delta \mathbf{m}_R$ and **m** is the 3×3 submatrix of **M**. As $\mathbf{m}_\Delta^T = \mathbf{m}_\Delta$ and $\mathbf{m}_\Delta^2 = \mathbf{m}'(\mathbf{m}')^T$, $\mathbf{m}_\Delta$ can be derived based on the Cayley-Hamilton theorem:

$$\mathbf{m}_\Delta = \pm\left[(\mathbf{m}')^T\mathbf{m}' + (\sqrt{\lambda_1\lambda_2} + \sqrt{\lambda_2\lambda_3} + \sqrt{\lambda_3\lambda_1})\mathbf{I}\right]\times\left[(\sqrt{\lambda_1} + \sqrt{\lambda_2} + \sqrt{\lambda_3})(\mathbf{m}')^T\mathbf{m}' + \sqrt{\lambda_1\lambda_2\lambda_3}\mathbf{I}\right], \tag{3-7}$$

where λ_1, λ_2 and λ_3 are the eigen values of $\mathbf{m}'(\mathbf{m}')^T$. The sign is the same as that of the determinant of **m**'. The total depolarization power Δ can be calculated as:

$$\Delta = 1 - \frac{|tr(\mathbf{m}_\Delta)|}{3}, \tag{3-8}$$

The submatrix $\mathbf{m}_R$ of the retardance matrix can then be derived as:

$$\mathbf{m}_R = \mathbf{m}_\Delta^{-1}\mathbf{m}' . \tag{3-9}$$

The Mueller matrix $\mathbf{M}_R$ for a retarder can be constructed from $\mathbf{m}_R$. And the total retardance R is calculated as the following:

$$R = \cos^{-1}\left[\frac{tr(\mathbf{M}_R)}{2} - 1\right]. \tag{3-10}$$

According to the method of Manhas *et al*., (2006) Ghosh and Wood (2008), the linear retardance can be further derived because the retardance matrix $\mathbf{M}_R$ can be represented as a combination of optical rotation R_C and linear retardance R_L. The linear retardance R_L can be obtained from the retardance submatrix $\mathbf{m}_R$ as (Ghosh and Wood, 2008):

$$R_L = \cos^{-1}\left(\sqrt{[\mathbf{m}_R(2,1) - \mathbf{m}_R(1,2)]^2 + [\mathbf{m}_R(1,1) + \mathbf{m}_R(2,2)]^2} - 1\right), \tag{3-11}$$

where $\mathbf{m}_R$(i, j) represents the ith row and jth column element of the retardance submatrix $\mathbf{m}_R$. The optical rotation is derived as:

$$2R_C = \tan^{-1}\left(\frac{\mathbf{m}_R(2,1) - \mathbf{m}_R(1,2)}{\mathbf{m}_R(1,1) + \mathbf{m}_R(2,2)}\right). \tag{3-12}$$

3.2 Results and Discussion

3.2.1 Polarization and Mueller Matrix Images

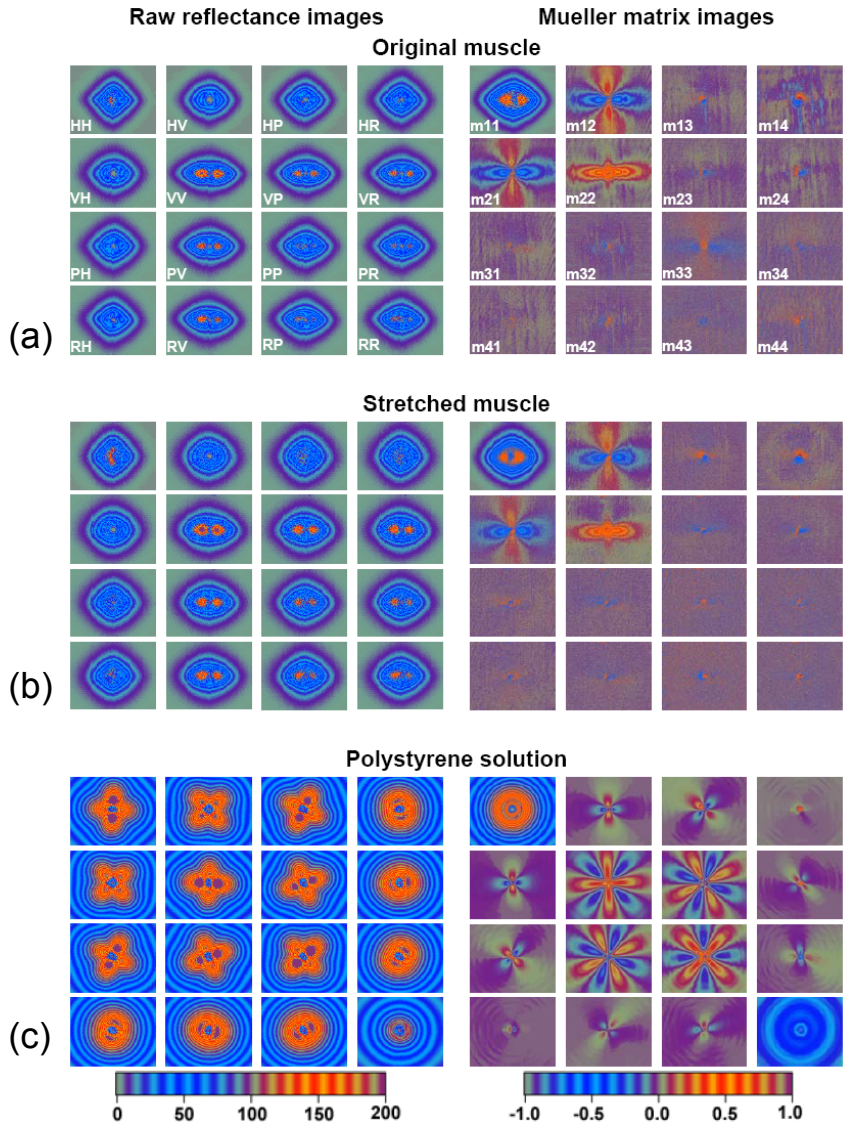

Fig. 3-2. Polarization reflectance images acquired in a muscle sample at its original length and when stretched 20% along the fiber orientation (vertical direction). As a comparison, images acquired in a solution of 1.093 μm polystyrenes (12%) are also shown. The image labels are the same as shown in the first sample.

Fig. 3-2(a) shows the raw polarization images of the muscle in its original length. The images are displayed using a banded pseudo-color map so that the equi-intensity profiles can be viewed easily. The muscle fiber was along the vertical direction (y-axis) in the image. The images are labeled using two letters: the first letter indicates the incident polarization and the second letter indicates the detection polarization. The 16 images reveal the unique rhombus-shaped reflectance patterns in skeletal muscles (Li, *et al*., 2008; Ranasinghesagara and Yao, 2007). The VV image has the largest intensity and the HH image shows the most significant diamond-like shape. The images in Fig. 3-2 have symmetric patterns along the diagonal direction. For example, the HV image is similar to the VH image and the PH image is similar to the HP image.

The calculated Mueller matrix images are very different in the muscle sample and the polystyrene solution. Only the four elements m_{11}, m_{12}, m_{21}, and m_{22} show strong signals in the muscle; while the polystyrene solution show prominent patterns in m_{22}, m_{23}, m_{32}, m_{33}. The exceptions are the m_{12} and m_{21} images, which appear similar in both samples. Stretching the muscle does not have a clear effect on the calculated Mueller matrix images.

As a comparison, polarization images of a polystyrene solution (1.09 μm, 0.12% concentration) are also shown in Fig. 3-2(c). The scattering coefficient μ_s and anisotropy of this solution were 44 cm^{-1} and 0.93, respectively. The images acquired in the polystyrene solution show different orientations depending on the incident and detection polarizations; while the images acquired in muscles are elongated primarily along the horizontal direction. However, the center parts of the VV image are all elongated in the same way in both samples.

3.2.2 Levenberg-Marquet Fitting Result

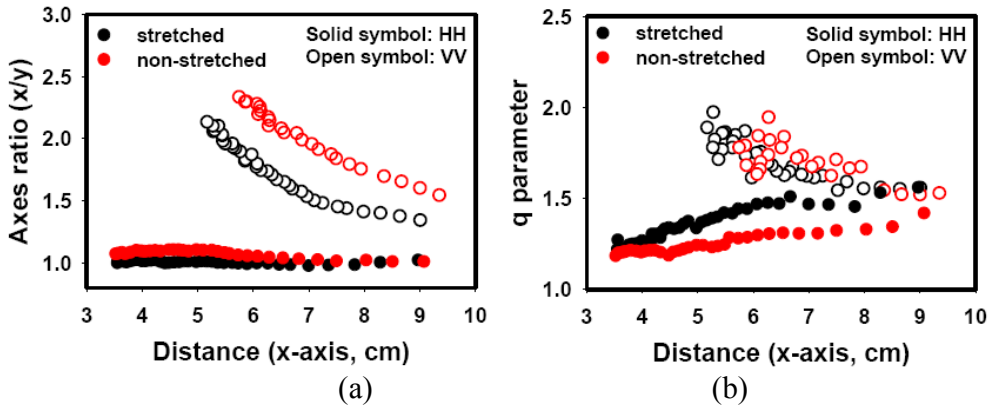

Fig. 3-3. The fitted (a) axes ratio and (b) q-parameter in the HH (solid symbols) and VV (open symbols) images.

When the muscle sample was stretched 20% along the muscle fiber direction, the polarization reflectance images overall had similar patterns. However, most polarization images seem to elongate along the stretching direction (the vertical direction). As the equi-intensity profiles are symmetric around the incident location, we applied a numerical fitting method to quantitatively describe the equi-intensity shapes. The fitting method (also used in section 2.2.2) has been described in detail elsewhere (Ranasinghesagara and Yao, 2007). Two fitting parameters can be derived: the axes ratio (l_x/l_y) and the shape parameter q, where l_x and l_y are the axis lengths of the equi-intensity profile extracted at a certain distance from the incident point. The shape parameter q=1 indicates a rhombus shape and q=2 indicates an ellipse. As shown in Fig. 3-3, stretching along the y-axis (muscle fiber direction) reduces the axes ratio in both HH and VV images. The VV image has a much larger change than the HH image. On the other hand, the q parameter is larger in the stretched HH image, indicating the equi-intensity shape has smoother corners. Similar trends exist in other images.

3.2.3 Diattenuation Images

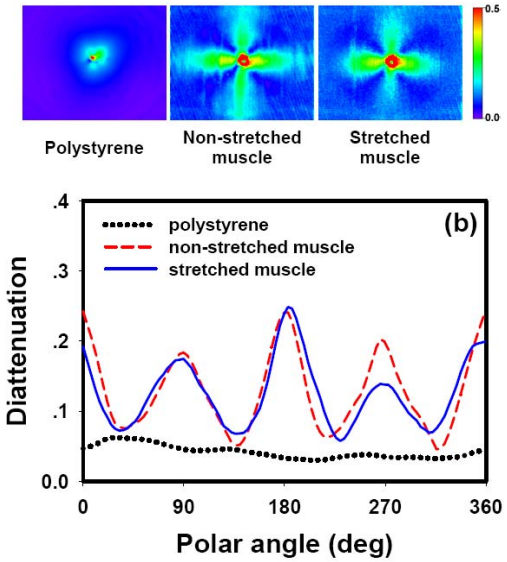

Fig. 3-4. Diattenuation images obtained in muscle and polystyrene solution. The diattenuation values shown in (b) were extracted at locations 5 mm away from the incidence.

Fig. 3-4 shows the diattenuation images extracted from the Muller matrix images using Eq. 3-5. Diattenuation indicates the signal intensity difference between two orthogonal polarization states and its value can be from zero to one. The images appear quite different the in muscle and the polystyrene solution. In the isotropic polystyrene solution, the diattenuation image has no clear pattern and the diattenuation values are close to zero at locations far away from incidence. However, the diattenuation images in muscle have a quatrefoil distribution with strong diattenuation along and perpendicular to the muscle fibers. The pattern along the muscle fiber direction has a smaller area than that perpendicular to the fibers.

Quantitatively, Fig. 3-4(b) shows the diattenuation values extracted at the sample surface located 5 mm away from the incident point. In the polystyrene solution, the diattenuation is less than 0.1 and does not change much with the polar angles. The

reflectance in muscle shows diattenuation values between 0.1 and 0.3. At locations perpendicular (0° and 180°) or parallel (90° and 270°) to the muscle fibers, the diattenuation is higher than at other locations. In addition, the values are higher at 0° and 180° than at 90° and 270°. Similar diattenuation patterns were observed in non-stretched and stretched muscles.

The diattenuation images in muscle are mostly determined by the m_{12} element because little information exists in the m_{13} and m_{14} components of the muscle Mueller matrix images. Therefore, the muscle diattenuation comes mostly from linearly diattenuation, specifically the "horizontal" diattenuation (Lu and Chipman, 1996). As can be seen in the raw reflectance images (Fig. 3-2), more V-polarized incident light is backscattered along the x-axis; while more H-polarized incident light is backscattered along the y-axis (muscle fiber direction). This phenomenon is consistent with the polarization-dependent sarcomere diffraction as discussed in Chapter 2. The sarcomeres diffract the majority of V-polarized light to the directions perpendicular to muscle fibers.

3.2.4 Depolarization Images

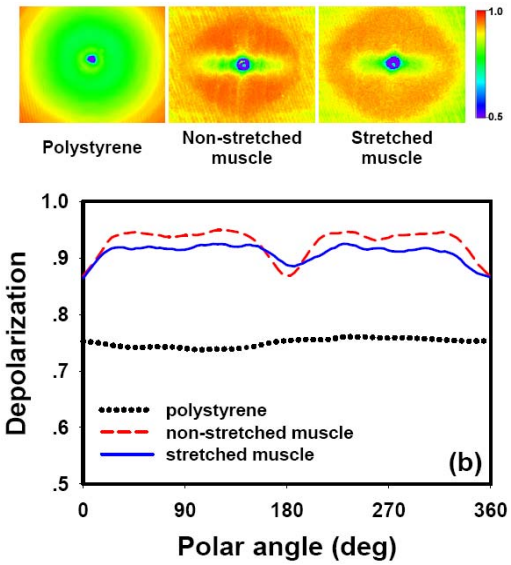

Fig. 3-5. Depolarization images obtained in muscle and polystyrene solution. The depolarization values shown in (b) were extracted at locations 5 mm away from the incidence.

The depolarization power describes the pure depolarizing capability of the medium. A depolarization value of one indicates the sample can completely depolarize the incident light. The extracted depolarization image in polystyrene solution (Fig. 3-5) shows a pattern with rotational symmetry. As the distance increases from the incident point, the depolarization value increases gradually from ~0.7 to close to one. The incident polarized light can be depolarized by multiple scattering. The polarization state is maintained better at locations close to the incident location because the probability of multiple scattering is smaller.

The muscle sample shows a strong anisotropic depolarization pattern. A large depolarization (>0.9) appears in the majority of the imaging area, which suggests that the muscle acts as an effective depolarizer. However, a small region along the x-axis

(perpendicular to the muscle fibers) shows smaller depolarization. This phenomenon is consistent with our previous observation (Li, *et al*., 2008) that the incident light maintains polarization better along the x-axis. Photons backscattered in this region likely experience fewer scattering events than other areas.

3.2.5 Retardance Images

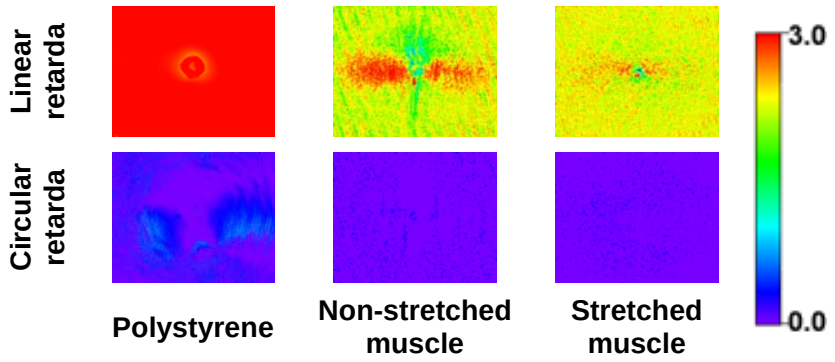

Fig. 3-6. Retardance images obtained in muscle and polystyrene solution.

The total retardance R is a combination of linear retardance and optical rotation. The retardance results appear to be much noisier than the diattenuation and depolarization components. This is attributed to the increasing computation error in the late stage of the decomposition procedure and the retardance matrix is calculated after the other two components (Hayes, 1997). As shown in Fig. 3-6, no significant optical rotation exists in either skeletal muscle or polystyrene solution. Therefore the measured retardance is primarily linear retardance. The decomposed total retardance in the polystyrene solution is approximately π. This phase difference between the two orthogonal polarization directions is attributed to the reflection geometry used in our study. Due to this π phase difference, a 45° linearly polarized (P) incident light becomes a -45° linearly polarized reflected light and right-hand circularly polarized (R) incident light becomes left-hand

circularly polarized reflected light.

In non-stretched muscle, the retardance is close to π only within a small area along the x-axis. In other words, within the region perpendicular to muscle fibers, the muscle acts similarly as a back-reflecting isotropic medium. Along the y-axis, the retardance values are smaller and approach $\pi/2$ when close to the incident point. In all other areas, the retardance is between $\pi/2$ and π. In stretched muscle, the retardance pattern along the x- and y-axis becomes insignificant. Both scattering (Ghosh and Wood, 2008) and birefringence (Pasquesi, *et al*., 2006) can produce the retardance observed in muscle. However, further studies are necessary to clarify their contributions.

3.3 Conclusion

We applied the polar decomposition algorithm to analyze the reflectance polarization Mueller matrix in skeletal muscle samples. The extracted diattenuation (D), retardance (R) and depolarization (Δ) in muscle are very different from those obtained in isotropic medium. The decomposed polarization images have strong anisotropic patterns along and/or perpendicular to muscle fibers, but rotationally symmetric patterns in the polystyrene solution. These anisotropic effects are related to the organized sarcomere structures in muscle. We found that stretching muscle along the fibers induced significant changes in the raw polarization-sensitive reflectance images. However, stretching induced minimal changes in the calculated Mueller matrix and the decomposed polarization images.

CHAPTER 4

POLARIZED TRANSMITTANCE IMAGING

4.1 Materials and Methods

4.1.1 Experimental Setup

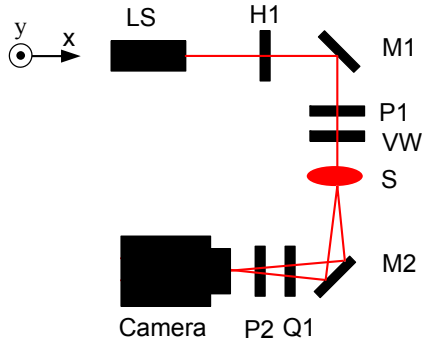

Fig. 4-1. The schematic of experimental setup. LS: a 10mW He-Ne laser; H1: half wave plate; M1: mirror; P1: polarizer; VW: variable waveplate; S: sample; M2: mirror; Q1: quarter waveplate; P2: polarizer; CCD: imaging camera.

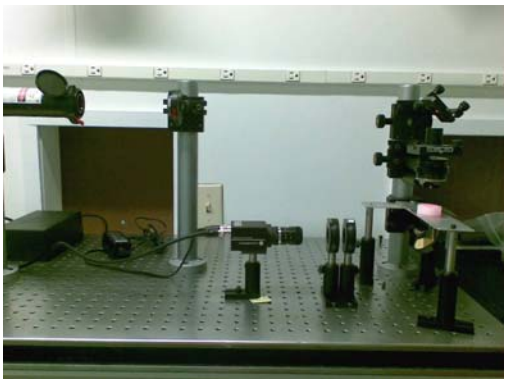

Fig. 4-2. Photo of actual experimental setup.

Our experimental setup was illustrated in Fig. 4-1. A polarized He-Ne laser was used as the light source. The laser light passed through a half-waveplate (HW) and a polarizer (P1). The incident power was adjusted by rotating the λ/2 waveplate. A variable waveplate (VW) was used to change the polarization states of the incident light. The transmitted light was imaged by a 16-bit CCD camera (PIXIS 512, Princeton Instruments, NJ) after passing through a λ/4 waveplate (QW) and a polarizer (P2). A zoom lens was used with the CCD camera and had an acceptance angle of 10.5°. The acquired image had a size of 512×512 pixels corresponding to an area of 16.4×16.4mm^2. To compensate the signal intensity changes at different sample thicknesses, both the CCD exposure time and incident light power were adjusted during the imaging process. Each image was averaged twenty times to improve signal to noise ratio.

To make the images smoother, we attached a small pager motor to the sample holder, which generates a very slight vibration (12000 rmp) during the experiment. The vibration will reduce the speckle noise and make the image appear smooth (Iwai, *et al*., 1982).

We used four different polarization incident states in the experiment: horizontal linearly polarized light (H), horizontal linearly polarized light (V), linearly polarized light 45^o to horizontal direction (P), right-handed polarized light (R). The whole setup was carefully calibrated with no sample (Baba, *et al*., 2002), and the measured extinction ratio for linearly polarized light and circularly polarized light were <-32 dB and <-30dB, respectively. The original thickness of the muscle was 12.0mm, and we cut it into 9.6mm, 8.7mm, 6.1mm, 5.2mm, 3.7mm, and 2.7mm for each measurement. The muscle was carefully placed along the direction of V polarization (y-axis) and immerged in the

relaxing solution. For each thickness, we acquired the images of the 16 states which is the combination of four different incident states and four different output states. For convenience, each polarization state was labeled with two letters: the first term stands for the incident polarization state and the second stands for the detection polarization state. For example, HV indicates the states with H-polarization incidents and V detection states. The Stokes vector and Mueller matrix can be calculated based on Eqs. 1-11 and 1-3.

We also studied the spatial distribution of the transmission images by analyzing the equi-intensity profiles. Such LM fitting algorithm was described in section 2.2.2. The polar decomposition method as discussed in section 3.1.2 was also applied to some of our results.

4.1.2 Calibration Process

The calibration of the input branch is the same with that of reflectance polarization imaging.

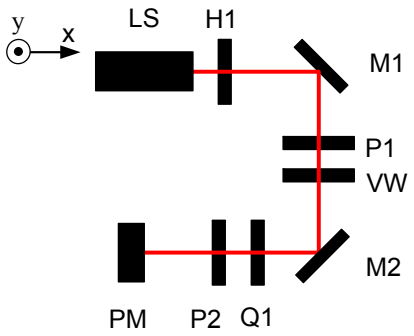

Fig. 4-3. Schematic of output calibration.

For the output branch (such as H, P, and R), arrange the setup like Fig. 4-3. The opposite input state (such as V, M, and L) should be adjusted first, and Q1 and P2 should

then be adjusted till the power meter (PM) reaches the minimum value. A reference coordinate system was defined as Fig. 4-4(a), and the direction corresponding to that of the system in the recorded images is as Fig. 4-4(b):

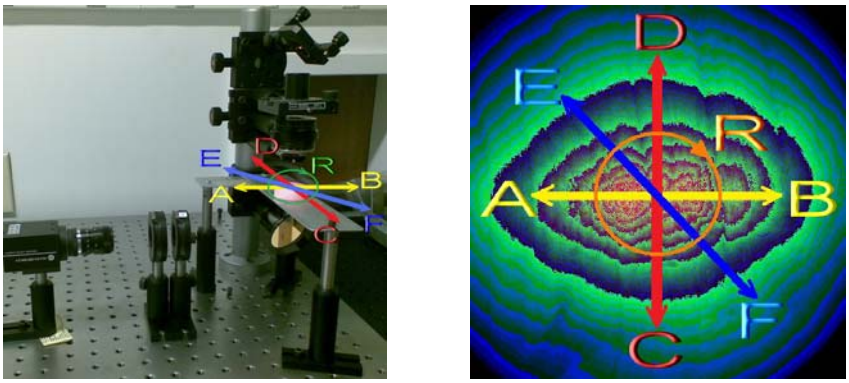

(a) (b)

Fig. 4-4. Directions defined in the system and recorded images.

4.1.3 Specimens

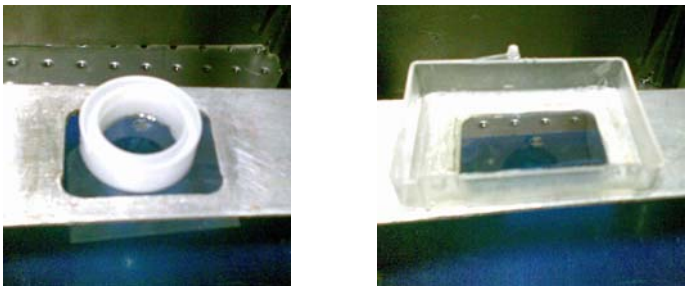

(a) (b)

Fig. 4-5. Sample containers for (a) scattering solution and (b) muscle slice.

a. Intralipid Solution

The 20% Intralipid® is a kind of fat emulsion which is clinically used as an intravenously administered nutrient (van Staveren, *et al*., 1991). Some times it is used as

a high scattering media to investigate light propagation in research studies. In our experiment, we used 20% Intralipid® solution (0.4% concentration by volume). It should be contained in a special container where the bottom is an optical glass as shown in Fig 4-5(a).

b. Polystyrene Solution

If the sample is the scattering solution, it should be contained in a special container where the bottom is an optical glass as shown in Fig 4-5(a). The concentration and particle size should be tested in order to get a clear pattern in the images. A little water should be applied between the sample holder and the container to avoid an interference pattern.

c. Muscle Slice

In our study, we used the Bovine *Sternomandibularis* muscle which was extracted right after slaughtering. The thickness of the raw muscle in the relaxed state was approximately 12.0 mm. The muscle sample was prepared to remove fat tissues from the surface and cut into a piece of 25.4 mm in length and width. The entire sample was immerged in a relaxing solution (Linari, *et al*., 1986; McDonald, *et al*., 1998) to prevent the rigor formation in a container (Fig 4-5(b)) with an optical transmitting bottom. The relaxing solution caused the crossbridge heads in muscle fiber to detach and therefore prevent the rigor-force (Linari, *et al*., 1986). To reduce sample thickness, a small layer was cut gradually from the original sample. The following seven thicknesses were used in this study: 12.0mm, 9.6mm, 8.7mm, 6.1mm, 5.2mm, 3.7mm, and 2.7mm.

4.2 Results and Discussion

4.2.1 Polarization Imaging Result

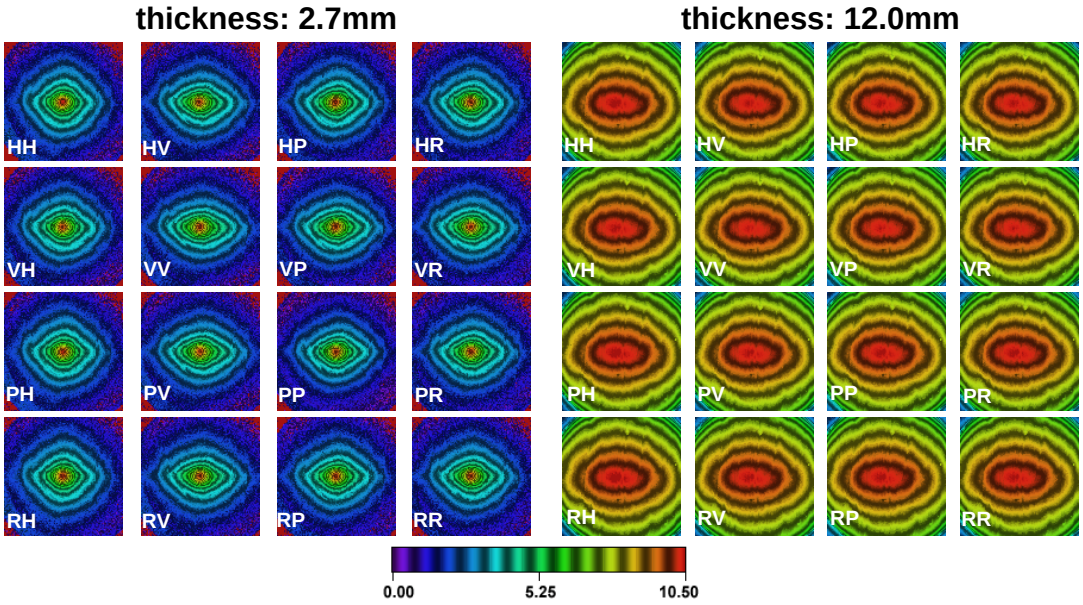

Fig. 4-6. Transmittance images measured with different combinations of incidence and detection polarizations in muscle samples of 12.0 mm and 2.7 mm thickness. The image shown has a size of 17.5×17.5 mm^2. The muscle fiber is oriented along the vertical direction and the H-polarization is along the horizontal direction. The raw images are shown in log-scales.

Fig. 4-6 shows the 16 transmittance images measured with different combinations of incident and detection polarization. The corresponding Mueller matrix images are shown in the right column in Fig. 4-6. Results shown were obtained in muscle samples of 12.0mm and 2.7 mm thickness. The muscle fiber was oriented along the vertical direction (y-axis) which is aligned with the vertical polarization. The equi-intensity image was shown in a pseudo-color, the same color stands for the same intensity.

In the 2.7 mm thick muscle, variations in spatial profiles can be seen in different polarization images. Specifically, the VV image is elongated along the x-axis; while the

HH image is somewhat equally distributed along the x- and y-axis. Other images show distributions between the HH and VV images. Such shape difference in the equi-intensity profiles gradually disappear in samples of larger thicknesses. As shown in Fig. 4-6, the polarization images obtained in a 12 mm thick sample are nearly identical.

4.2.2 Levenberg-Marquet Fitting Result

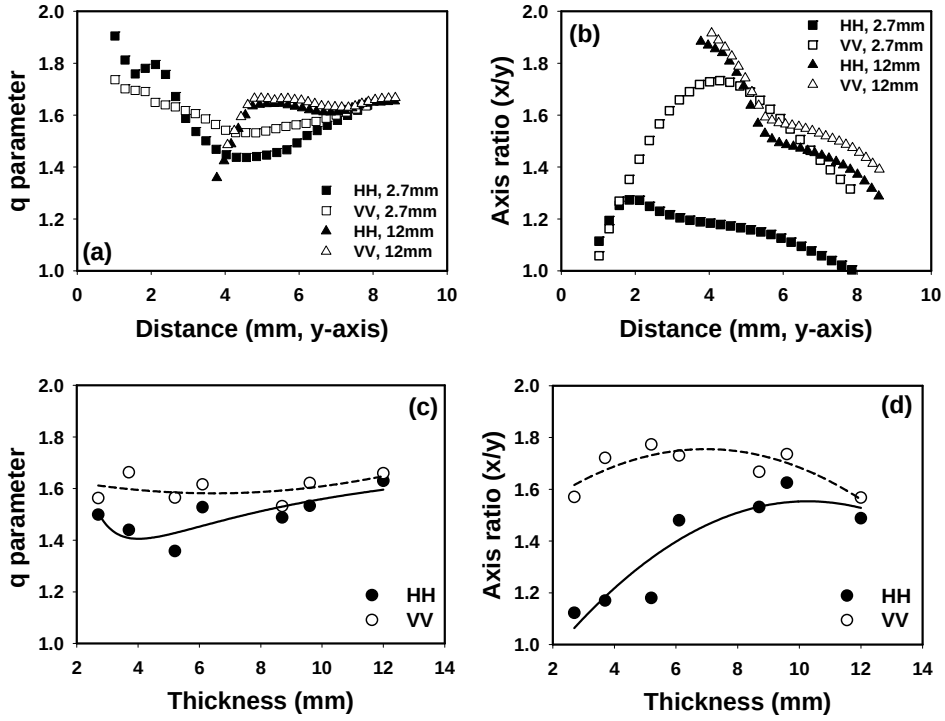

Fig. 4-7. Fitted (a) q and (b) Axis ratios (x/y) at difference distances from the incident point measured in HH and VV images obtained in muscle samples of 12.0 mm and 2.7 mm thickness. At fixed distance of 6 mm from the incident point, the graphs (c) and (d) show the fitted q and axis ratios (x/y) in muscle samples of different thicknesses.

To quantify the equi-intensity profiles, Eq. 2-1 was used to fit all acquired raw polarization images. The results confirm the observation in Fig. 4-6 that the equi-intensity

profiles in HH and VV images represent two extreme cases and the other images have profiles between them. In the 2.7 mm thick sample, the q parameters are ~1.8 at ~1.0 mm to the incident point and decrease thereafter with the distance (Fig. 4-7(a)). It reaches a minimal at ~ 4.0 mm to the incident and starts to increase. At larger distances from the incident, the fitted q parameters are identical in HH and VV images; while the VV image has higher q values than the HH image at distances between 3~7 mm from the incidence. This is consistent with the observation that the equi-intensity profile in the HH image is closer to a rhombus. In the 12 mm sample, the equi-intensity profiles at small distances (<4 mm) are irregular and lead to incorrect fitting. However, the fitted q values are stable starting at 4 mm from the incident, and the HH and VV images have essentially the same q values.

The fitted axis ratios (x/y) are also similar in the HH and VV images obtained in the 12 mm sample (Fig. 4-7(b)). Considering the similar q values, this result indicates that the equi-intensity profiles have almost identical shapes in the HH and VV images in the 12 mm thick sample. The fitted axis ratios (x/y) decrease from ~1.9 at 4.0 mm distance to ~1.4 at 8.5 mm distance, suggesting the profile becomes less elongated along the x-axis (perpendicular to muscle fibers) with the evaluation distance.

In the 2.7 mm thick sample, the fitted axis ratios (x/y) are very different in the HH and VV images except for those measured at small distances. The axis ratios (x/y) approach 1.0 in both HH and VV images when measured at distances close to the incident point (~1 mm). Taking consideration of the large q value (Fig. 4-7(a)), these results indicate a circular beam profile at small distances. At distances larger than 2 mm, the axis ratios (x/y) in the VV image are significantly larger than those in the HH image.

In other words, the equi-intensity profiles in the VV image are more elongated along the x-axis (perpendicular to muscle fibers). In both HH and VV images, the axis ratios (x/y) initially increase with distance, reach a maximal value, and decrease with distance thereafter. Therefore, the equi-intensity profile becomes less anisotropic at large distances from the incidence.

In the thinnest sample (2.7mm), at very small distance to the incident (~1mm), the profiles of both HH and VV showed a circular pattern which was the shape of incident. That means the ballistic transmitted light was dominant in this region. With the distance going to 4mm, the q value of HH and VV followed the same decreasing trend and the difference in axis ratios (x/y) began to increase. The shape of the profiles became diamond-like, and the ratio of two axes was very different at 4mm. That is because the diffraction effect of muscle sarcomere (Sidick, *et al*., 1992) started to play a role in light propagation. After that, the q value began to increase and finally reached 1.6 at (~8mm) and the B parameter then decreased. The change of the B parameter in the profiles was caused by the cylinder structure of muscle fiber (Klenle, *et al*., 2003; Ranasinghesagara and Yao, 2007). Also, the multiple scattering effect became dominant at the same time.

In thick samples, at ~ 4mm to the incident point, the q value of HH and VV also increased along the distance, but more dramatically than that in the thin sample. That is because the multiple scattering effect was much stronger in thick muscles than in thin muscles. Starting from ~5mm, the q value became stable at 1.6 and the decrease of the B parameter becomes slower which indicates that the multiple scattering is dominant. Also, the difference of B and q parameter for HH and VV at all distances was very small. In other words, the profiles were almost the same for different polarization states. That is

caused by the depolarization effect from multiple scattering.

Fig. 4-7(c) and Fig. 4-7(d) show the q and axis ratios (x/y) obtained in samples of different thicknesses. The values were measured at a fixed distance of 6 mm from the incident point. Overall, the q parameters have small variations between 1.4 ~ 1.7 in samples of 2.7 - 12 mm thick. The difference in q values between HH and VV images is very small in thick samples. Similarly, the difference in axis ratio between HH and VV images diminishes with sample thickness. Both q and axis ratios (x/y) have much smaller variations with sample thickness in the VV image than in the HH image. This is because the average optical pathlength increased with sample thickness. Therefore the incident light was depolarized during multiple scattering, and the profiles became stable relative to thickness.

4.2.3 Transmittance Intensity

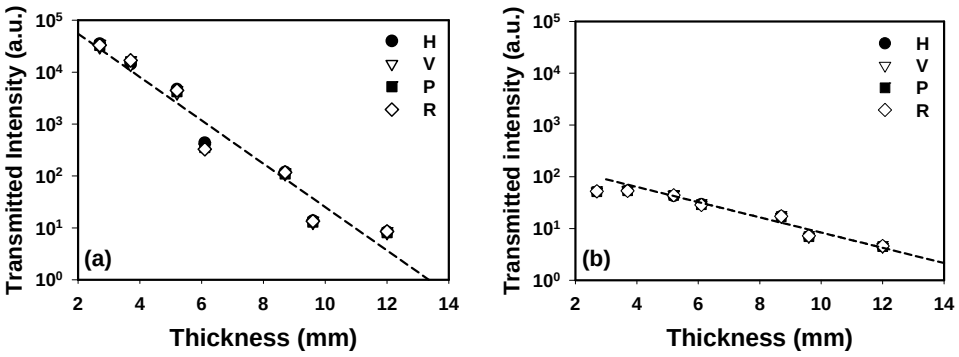

Fig. 4-8. The unpolarized total transmitted intensity measured with different incident polarization in samples of different thickness. (a) Intensity averaged within 1 mm (30 pixels) diameter from the incidence. (b) Intensity averaged within an area that is between 2.05 mm (60 pixels) and 6.84 mm (200 pixels) from the incident location.

Overall, the transmitted light intensity decreases with sample thickness. As shown in Fig. 4-6, the transmitted light covers a large area even with a point incident light. To quantitatively study the change of transmission with sample thickness, we divided the image area into two regions. The first region covers an area that has a radius of 15 pixels (~ 0.5 mm) from the incidence; and the second region covers an area with a radius between 60 and 200 pixels (2.05 – 6.84 mm) from the incidence. The transmitted light intensity was calculated by averaging pixel counts with the specific region. All intensities were normalized by dividing the exposure time and incident power for the corresponding incident polarization.

Because of the small incidence beam size (~1 mm), transmitted light in the second region must be scattered. On the other hand, transmitted light within the first region may be consisted of both non-scattered and scattered components. The scattered component increases with thickness. To estimate the scattered light intensity within the first region, the transmittance within the second region was fitted with a two dimensional Gaussian function which was extrapolated to the first region to estimate scattering contribution. The extrapolated values were then deducted from the intensities measured within the first region. We found the scattering contribution is only significant at the last two thicknesses (9.7 mm and 12 mm) within the first region.

As shown in Fig. 4-8, the ballistic component decreases nearly exponentially with the sample thickness. The fitted attenuation coefficient is 0.42 mm^{-1} (R^2 =0 .94). The scattered light has little change in intensities up to ~ 5 mm thickness. It starts to decrease exponentially thereafter, but at a slower rate of 0.15 mm^{-1} (R^2 =0 .95). Since the scattering effect of the second region is much more than that of the first region, so that

the extinction of transmitted light is more than that in the first region.

4.2.4 DOP Values

Fig. 4-9 (1) shows the measured DOP in samples of different thicknesses. Similarly to Fig. 4-8, the results were calculated separately in the ballistic region and the scattering region.

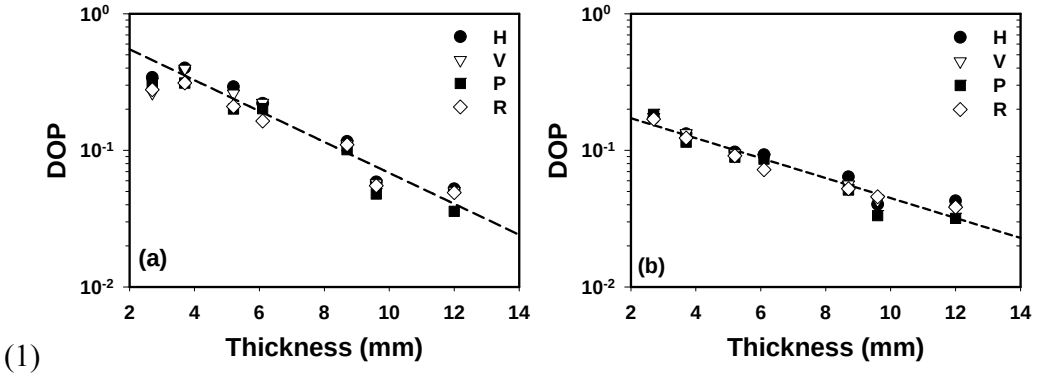

(1)

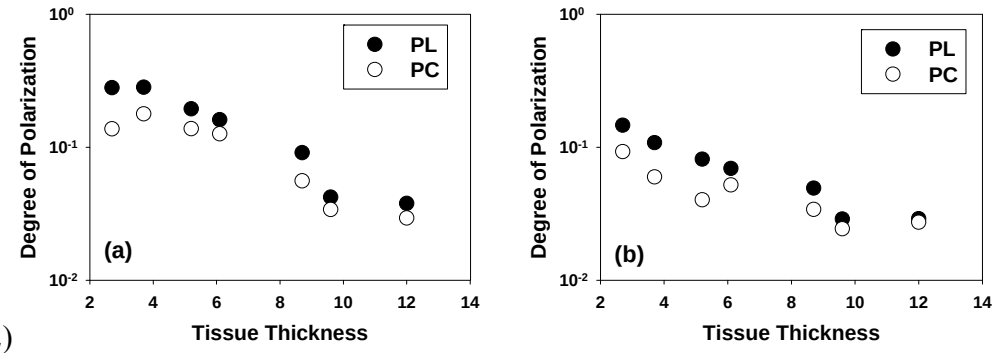

(2)

Fig. 4-9. (1): The degree of polarization (DOP) changing with sample thickness and measured with different incident polarization. (a) Results averaged within 1 mm (30 pixels) diameter from the incidence. (b) Results averaged within an area that is between 2.05 mm (60 pixels) and 6.84 mm (200 pixels) from the incident location. (2): The degree of linear and circular polarization beef muscle as a function of the tissue thickness. The muscle fiber was oriented along vertical direction, and the incident is horizontal linearly polarized light. (a) Results averaged within 1 mm (30 pixels) diameter from the incidence. (b) Results averaged within an area that is between 2.05 mm (60 pixels) and 6.84 mm (200 pixels) from the incident location.

The DOP decreases almost exponentially. However, the DOP of the ballistic component decreases much faster than the scattered component. The fitted decay rates were 0.11 mm^{-1} and 0.07 mm^{-1} for the ballistic and scattered components, respectively. It is interesting to note that these decay rates are much smaller than those of the corresponding intensities described in the previous paragraph. As the photons experience less scattering in the ballistic (central) area, the polarization states remain better than in the scattering area. That is why the DOP of the central area in thin tissue is much larger than in the surrounding area; with the thickness increasing, the depolarization effect of the tissue tends to mainly affect the DOP, and the DOP between the two parts reduces to a similar value.

Fig. 4-9 (2) shows the measured DOLP and DOCP of horizontal linearly polarized incident in samples of different thicknesses. They follow a similar trend as in Fig. 4-9 (1). An interesting phenomenon is that the circular polarization component can be detected, and it is always smaller than the linear polarization component. This is caused by the birefringent effect of muscle fibers (Sankaran, *et al*., 2002).

4.2.5 Mueller Matrix Images

Fig. 4-10 shows the Mueller matrix images calculated from the raw images (Fig. 4-6) using Eq. 1-3. In the 12 mm thick sample, no clear patterns are seen in the Mueller matrix. All elements (except for M_{11}) are essentially blank images with values close to zero. However, in the 2.7 mm thick sample, M_{12} and M_{21} elements show clearly cross-like patterns as observed in our previous reflectance measurements (Li, *et al*., 2008). That means in 12mm thickness tissue, the incident light is almost depolarized.

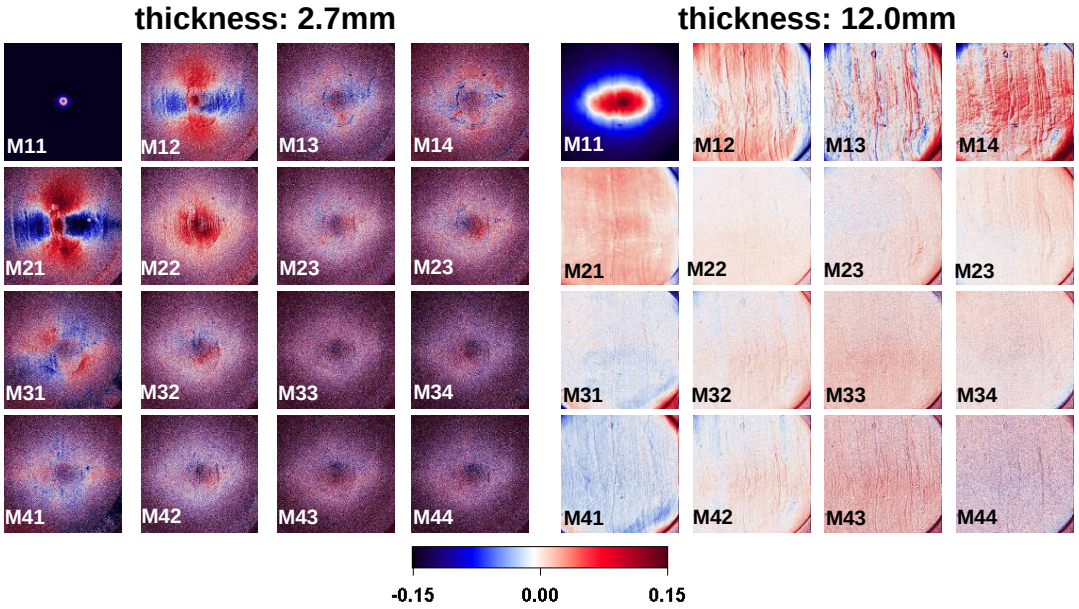

Fig. 4-10. The diattenuation, depolarization, and retardance obtained using polar decomposition in samples of different thicknesses. (a) Results averaged within 1 mm (30 pixels) diameter from the incidence. (b) Results averaged within an area that is between 2.05 mm (60 pixels) and 6.84 mm (200 pixels) from the incident location.

4.2.6 Polar Decomposition Result

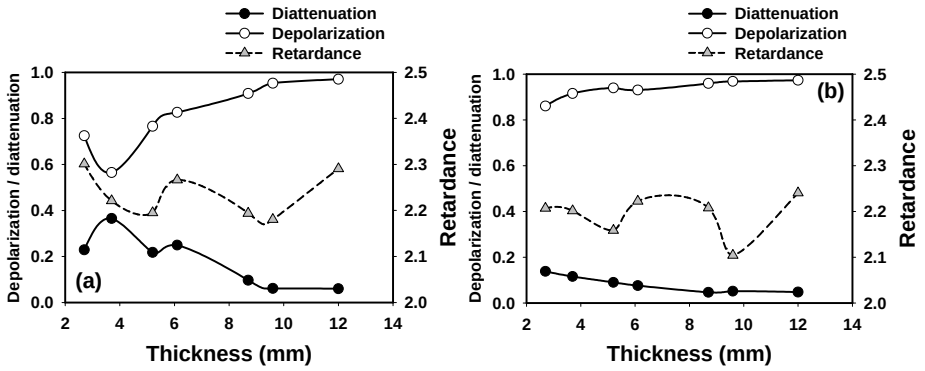

Fig. 4-11. The diattenuation, depolarization, and retardance obtained using polar decomposition in samples of different thicknesses. (a) Results averaged within 1 mm (30 pixels) diameter from the incidence. (b) Results averaged within an area that is between 2.05 mm (60 pixels) and 6.84 mm (200 pixels) from the incident location.

Polar decomposition algorithm (see section 3.1.2) was applied to extract quantitative diattenuation, depolarization, and retardation values from the measured Mueller matrix images. The calculation was conducted separately in the ballistic region and the scattering region. As shown in Fig. 4-11, with the tissue thickness increasing, the diattenuation of the central part decreases from ~0.36 to ~0.06; that of the surrounding part decreases from ~0.14 to ~0.05. That means the dependence on the incident polarization state of the transmitted light is more in ballistic area than in surrounding area, especially in thin sample. And, for the depolarization coefficient, with the tissue thickness getting larger, the depolarization of the central part increases from ~0.56 to ~0.97; that of the surrounding part increases from ~0.86 to ~0.97. This means the depolarization capability increases via sample thickness and that of the central part is stronger than the surrounding part.

The curve of retardance is very interesting. For different thicknesses, the retardance of the central part varies from ~2.2 to ~2.3, and that of the surrounding part varies from ~2.1 to ~2.2. Both of them have some fluctuation in between. Due to the periodic sarcomere structure, muscle can be treated as optical grating. Such fluctuation of retardance may be caused by the phase difference of the different thickness of the grating.

4.2.7 Polarization Transmittance Imaging of Polystyrene

Fig. 4-12(a) shows the transmittance polarization images of the 0.015% concentration with a 0.365 μm particle size and the sample thickness was 11mm. Each image is the average of 40 images with an interval of 20 ms. The incident point is at the center, and the images are also shown in a pseudo-color depiction of the equi-intensity

distribution. From the 16 combinations of the polarization states, we can see a diagonal symmetric relationship between incident polarization and detection polarization can be identified from the images. For example, HV and VH are almost identical to each other. So we just need to describe part of these images such as HH, VH, VV, PH, PV, PP, RH, RV, RP and RR. VH shows a square-like shape with a small distance to the incident point with very weak intensity. RR shows a set of circular profiles with the same center. Other images we need to describe have the profiles of ellipse. HH, VV and PP have stronger signals than other images, the long axes of which are along y-axis, x-axis and -45^{o} to x-axis. The long axes of the ellipse profiles in RH, RV, and RP are also along y-axis, x-axis and -45^{o} to x-axis.

The Mueller matrix images (Fig. 4-12(b)) of the polystyrene (Polysciences, Inc., Warrington, PA) solution are also shown. The diameter of the polystyrene sphere was 0.365 μm. A volume concentration of 0.015% was used in the study with a calculated scattering coefficient of 2.09 cm^{-1} and anisotropy of 0.73. The Mueller matrix images obtained in the polystyrene solution are similar as those approximated before (Tuchin, *et al*., 2006). The M11 component of the Mueller matrix represents the unpolarized measurements. As expected, the equi-intensity profiles of the M11 element in the polystyrene solution are a set of circles centered at the incident point with the transmittance intensity decreasing with the radial distance. M22, M33 and M33 elements also show very strong signals. M22 shows a spindle shape with a large distance to the center, M33 shows a rhombus shape with a long axis -45^{o} to x-axis and M44 shows a set of circular shapes with the same center. The equi-intensity profiles of the M12 and M21 elements in the polystyrene solution have similar shapes of quatrefoils. The intensity

values along the x-axis are negative, and those along the y-axis are positive. A close examination indicates that the intensity distributions along the x- and y-axis are similar in the polystyrene solution. The profiles in M13 and M31 also have similar quatrefoils shapes, with positive and negative pairs -45° and +45° to x-axis, respectively. We can not see clear patterns in other elements.

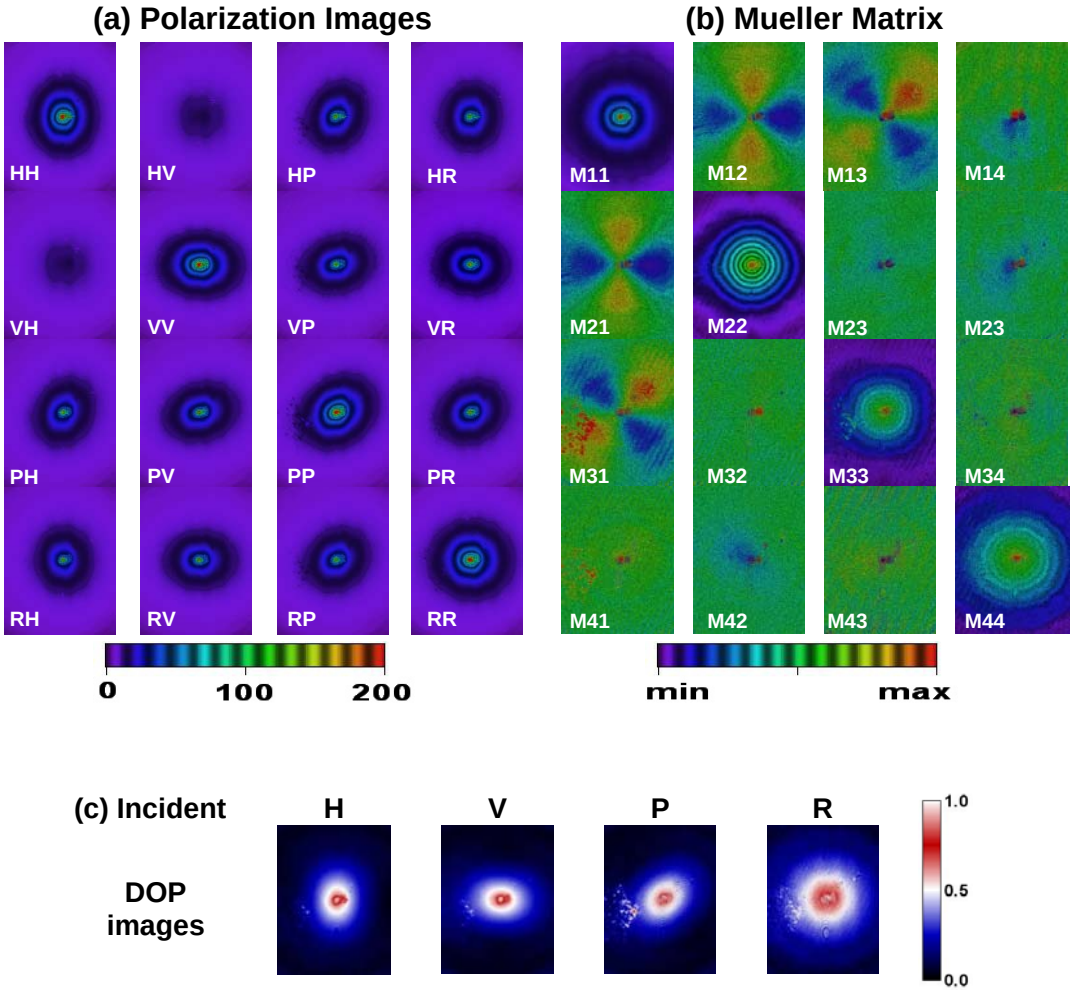

Fig. 4-12. (a) Polarization-sensitive transmittance images and (b) Mueller matrix and (c) DOP images in 2.63% polystyrene solution with 0.015% concentration. The diameter of the polystyrene particles is 0.365 μm, and the thickness of the solution is 11mm. The optical parameter of the solution is μ_a =0, μ_s =2.09cm^{-1}, g=0.73, μ_s' =0.57cm^{-1}. The image size was 23.7mm by 17.8mm. The H-polarization direction was along the horizontal direction.

Fig. 4-12(c) shows images of the degree of polarization (DOP) of transmittance images in 2.63% polystyrene solution with 0.015% concentration calculated from the Stokes vector images by using Eq. 1-2. The H-polarization direction was along the horizontal direction. As shown in Fig. 4-12(c), the DOP images with H, V and P incident show the ellipse shapes with the long axis of y-axis, x-axis and -45^{o} to x-axis, respectively . With linearly polarized incident light, the transmitted light in the polystyrene solution maintains a certain polarization along the direction orthogonal to the original polarization direction.

The above phenomenon can be explained by the Mie scattering theory of sphere particles. And it can be a great example as a comparison of former muscle transmittance experiments.

4.3 Conclusion

The polarization-sensitive transmittance images in fresh bovine *sternomandibularis* muscle with different thickness were acquired. They show very different patterns from those of the polystyrene solution. A quantitative analysis (LM fitting) of the imaging profiles was applied and the Mueller matrix images were computed. We also calculated the relative transmittance intensity, DOP values and polar decomposition components of the ballistic transmitted area and diffuse area with different thickness. By analyzing those experimental results, we can see that the propagation of polarized light through muscle is very different from that through the isotropic media. Those differences are because of the uniquely anisotropic structure of skeletal muscle. The scattering effect of tissue scatterers, the birefringence from the fibrous structure, the

scattering from the cylindrical fibers and the sarcomere diffraction may all contribute to the results we have received. It is difficult to explain the phenomenon using only one theory, so more experiments are needed in order to understand how different structures in skeletal muscle affect the propagation of polarized light. Such studies may have a great contribution in medical diagnosis or food quality control.

CHAPTER 5

SUMMARY AND FUTURE DIRECTION

Based on the research, we found that a fresh skeletal muscle shows very different polarization-sensitive reflectance and transmittance profiles from those from isotropic media. These results indicate that in addition to the multiple scattering by tissue scatterers, the muscle fiber induced birefringence and sarcomere induced diffraction also contribute to the reflectance profiles and intensity distribution in the Mueller matrix and DOP images. A sarcomere diffraction model revealed that the grating effect of skeletal muscle can explain the x-axis preference of our results.

The polar decomposition method has been applied to extract polarization parameters from the reflectance Mueller matrix images of stretched and released muscle. Stretching the muscle induced changes in the axis ratio of the equi-intensity profiles in the raw polarization images. However, it did not have a great effect on the diattenuation, depolarization and retardance coefficients.

The transmittance polarization imaging on skeletal muscle was also studied. As expected, the results show different profiles from those obtained in the polystyrene solution. The imaging was conducted in muscle slices of different thicknesses to study the thickness effect in polarization transmittance. Those differences were associated with the uniquely anisotropic structure of skeletal muscle. The scattering effect of tissue

scatterers, the birefringence of the fibrous structure, the scattering of cylindrical fibers and the diffraction of sarcomere may all contribute to the results we have received.

Further analysis of our results and more experiments are still needed for us to understand the mechanism of polarized light propagation in skeletal muscle. The differences of skeletal muscles from different parts of the body need to be considered in order to develop a model of polarized light propagation inside different skeletal muscle. Meanwhile, the effects of the skin and fat tissue on top of skeletal muscle need to be investigated so that a model of light propagation in multi-layer tissue can be developed. At that stage, the non-invasive polarization optical technique can further be applied to animals or humans to assist the diagnosis of muscle diseases.

APPENDIX

Matlab Code for Polar Decomposition Method

```
% % Polar Decomposition Algorithm
% % Author: Xin Li
% % xlm72@mizzou.edu
% % University of Missouri
% % S. manhas' method is based on
% % 'Mueller matrix approach for determination of optical rotation in chiral
% % turbid media in backscattering geometry'.
% % Polar Decomposition Algorithm
% % Author: Xin Li
% % xlm72@mizzou.edu
% % University of Missouri
% % S. manhas' method is based on
% % 'Mueller matrix approach for determination of optical rotation in chiral
% % turbid media in backscattering geometry'.

work_dir = cd;
MM_dir = uigetdir('F:\Xin research\Xin experiment result');
cd(MM_dir);               %Open object directory
mkdir('Polar_decomposition');
Pol_dir = sprintf('%s\\Polar_decomposition',MM_dir);
cd(MM_dir);               %Make output directory
Img_W = 512;
Img_H = 512;              %Define image size

load M11.txt
load M12.txt
load M13.txt
load M14.txt
load M21.txt
load M22.txt
load M23.txt
load M24.txt
load M31.txt
load M32.txt
load M33.txt
load M34.txt
load M41.txt
load M42.txt
load M43.txt
load M44.txt      % Load unnormalized Mueller matrix files

for i = 1:Img_W
    for j = 1:Img_H

        if M11(i,j)==0
            M11(i,j)=eps;
        end
```

```
        M(1,1) = 1;
        M(1,2) = M12(i,j)/M11(i,j);
        M(1,3) = M13(i,j)/M11(i,j);
        M(1,4) = M14(i,j)/M11(i,j);
        M(2,1) = M21(i,j)/M11(i,j);
        M(2,2) = M22(i,j)/M11(i,j);
        M(2,3) = M23(i,j)/M11(i,j);
        M(2,4) = M24(i,j)/M11(i,j);
        M(3,1) = M31(i,j)/M11(i,j);
        M(3,2) = M32(i,j)/M11(i,j);
        M(3,3) = M33(i,j)/M11(i,j);
        M(3,4) = M34(i,j)/M11(i,j);
        M(4,1) = M41(i,j)/M11(i,j);
        M(4,2) = M42(i,j)/M11(i,j);
        M(4,3) = M43(i,j)/M11(i,j);
        M(4,4) = M44(i,j)/M11(i,j);          %normalize mueller matrix

        m = M(2:4,2:4);
        Dvec = ([M(1,2) M(1,3) M(1,4)]')/M(1,1);
        D(i,j) = sqrt(M(1,2)^2+M(1,3)^2+M(1,4)^2)/M(1,1);   %Diattenuation

        if D(i,j)==0
            D(i,j)=eps;
        end

        Dnorm = Dvec/D(i,j);
        I = [1 0 0;0 1 0; 0 0 1];
        mD = sqrt(1-D(i,j)^2)*I+(1-sqrt(1-D(i,j)^2))*Dnorm*Dnorm';
        MD = [1 Dvec'; Dvec mD];
        Mprim = M*pinv(MD);
        mprim = Mprim(2:4,2:4);

        for i1 = 1:3
            for j1 = 1:3
                if mprim(i1,j1)==0
                    mprim(i1,j1) = eps;
                end
            end
        end

        Pvec = ([M(2,1) M(3,1) M(4,1)]')/M(1,1);
        Pdelta = (Pvec-m*Dvec)/(1-D(i,j)^2);
        lamda= eig(mprim*mprim');
        ll(i,j)=sum(eig(mprim*mprim'));
        mdelta  =  sign(det(mprim))*pinv(mprim*mprim'+(sqrt(lamda(1)*lamda(2))+...

sqrt(lamda(2)*lamda(3))+sqrt(lamda(3)*lamda(1)))*I)*((sqrt(lamda(1))+...
            sqrt(lamda(2))+sqrt(lamda(3)))*mprim*mprim'+...
            sqrt(lamda(1)*lamda(2)*lamda(3))*I);
        Mdelta = [1 0 0 0; Pdelta mdelta];     % Depolarization matrix
        mR = pinv(mdelta)*mprim;
        z = [0;0;0];
        MR = [1 0 0 0;z mR ];           % Retardance matrix
        R(i,j) = acos(trace(MR)/2-1);
        if R(i,j)==0;
            R(i,j) = eps;
        end
        R = real(R);                    % Total Retardance
        r3 = (1/(2*sin(R(i,j))))*(mR(1,2)-mR(2,1));
        r2 = (1/(2*sin(R(i,j))))*(mR(3,1)-mR(1,3));
        delta(i,j) = 1-abs(trace(mdelta)/3);         % Depaloarization coef
```

```
        deltatest(i,j) = 1 - sqrt(sum(sum((M.*M)))-1)/sqrt(3);
        cr = cos(R(i,j)/2);
        sdelta(i,j) = 2*acos(sqrt(r3^2*(1-cr^2)+cr^2));
        sdelta(i,j) = real(sdelta(i,j));             % Linear retardance
(Manhas)
        phy(i,j) = acos(cr/cos(sdelta(i,j)/2));
        phy(i,j) = real(phy(i,j));
        if r2==0
            r2=eps;
        end
        sdelta2(i,j) = acos(sqrt((MR(2,2)+MR(3,3))^2+...
            (MR(3,2)-MR(2,3))^2)-1);
        sdelta2(i,j) = real(sdelta2(i,j));          % Linear retardance (Ghosh)
        MR2233 =MR(2,2)+MR(3,3);

        if MR2233==0;
            MR2233=eps;
        End

        phy2(i,j) = 0.5*atan((MR(3,2)-MR(2,3))/MR2233);
        phy2(i,j) = real(phy2(i,j));
        Romatri = [1 0 0 0;
            0 cos(2*phy(i,j)) sin(2*phy(i,j)) 0;
            0 -sin(2*phy(i,j)) cos(2*phy(i,j)) 0;
            0 0 0 1];
        MLR = MR*pinv(Romatri);
        mLR = MLR(2:4,2:4);
        if mLR(1,3)==0;
            mLR(1,3) = eps;
        end
        mLR2332 = mLR(2,3)-mLR(3,2);
        if mLR2332==0;
            mLR2332=eps;
        end
        sita2(i,j) = atan((mLR(3,1)-mLR(1,3))/mLR2332);
        if sita2(i,j) < 0
            sita2(i,j) = pi + sita2(i,j);
        end

        sita2(i,j) = real(0.5*sita2(i,j));
    end
end
cd(Pol_dir);
save sdelta_Manhas.txt sdelta -ascii
save phi_Manhas.txt phy -ascii
save delta.txt delta -ascii
save d.txt D -ascii
save R.txt R -ascii
save sdelta_Ghosh.txt sdelta2 -ascii
save phi_Ghosh.txt phy2 -ascii
save sita_Ghosh.txt sita2 -ascii
cd(work_dir);
```

REFFERENCES

Baba, J. S., Chung, J.-R., DeLaughter, A. H., Cameron, B. D., & Cote, G. L. (2002). Development and calibration of an automated Mueller matrix polarization imaging system. *J. Biomed. Opt., 7* (3), 341-349.

Backman, V., Gurjar, K., Badizadegan, K., Itzkan, I., Dasari, R. R., Perelman, L. T., & Feld, M. S. (1999). Polarized light scattering spectroscopy for quantitativemeasurement of epithelial cellular structures in situ. *IEEE J. Quantum Electron., 5* (4), 1019-1026.

Berne, R. M., & Levy, M. N. (1992). *Physiology* (3rd Edition.): Mosby Year Book, 1085p.

Bickel, W. S., Davidson, J. F., Huffman, D. R., & Kilkson, R. (1976). Application of polarization effects in light scattering: A new biophysical tool. *Proc. Nat. Acad. Sci. USA, 73* (2), 486-490.

Bohren, C. F., & Huffman, D. R. (1983). *Absorption and Scattering of Light by Small Particles*. New York: Wiley, 544p.

Chung, J., Jung, W., Hammer-Wilson, M. J., Wilder-Smith, P., & Chen, Z. (2007). Use of polar decomposition for the diagnosis of oral precancer. *Appl. Opt., 46* (15), 3038-3045.

Demos, S. G., & Alfano, R. R. (1997). Optical polarization imgaing. *Appl. Opt., 36* (1), 150-155.

Demos, S. G., Savage, H., Heerdt, A. S., Schantz, S., & Alfano, R. R. (1996). Time resolved degree of polarization for human breast tissue. *Optics Comm., 124* (5-6), 439-442.

Deng, Y., Zeng, S., Lu, Q., Zhu, D., & Luo, Q. (2007). Characterization of backscattering Mueller matrix patterns of highly scattering media with triple scattering assumption. *Opt. Express, 15* (15), 9672-9680.

Doit (2006). Polarization Retrieved March 25, 2009, from http://en.wikipedia.org/wiki/Polarization

Ghosh, N., & Wood, M. F. (2008). Mueller matrix decomposition for extraction of individual polarization parameters from complex turbid media exhibiting multiple scattering, optical activity, and linear birefringence. *J. Biomed. Opt., 13* (4), 044036.

Hayes, D. M. (1997). Error propagation in decomposition of Mueller matrices. *Proc. SPIE, 3121* (1), 112-123.

Hielscher, A. H., Eick, A. A., Mourant, J. R., Shen, D., Freyer, J. P., & Bigio, I. J. (1997). Diffuse backscattering Mueller matrices of highly scattering media. *Opt. Express, 1* (13), 441-453.

Itoh, M., Yamanari, M., Yasuno, Y., & Yatagai, T. (2005). Polarization characteristics of multiple backscattering in human blood cell suspensions. *Optical and Quantum Electronics, 37*, 1277-1285.

Iwai, T., Takai, N., & Asakura, T. (1982). Dynamic statistical properties of laser speckle produced by a moving diffuse object under illumination of a Gaussian beam. *J. Opt. Soc. Am., 72* (4), 460-467.

Jacques, S. L., Roman, J. R., & Lee, K. (2000). Imaging superficial tissues with polarized light. *Lasers in Surgery and Medicine* (26), 119-129.

Jacques, S. L., Ramella-Roman, J. C., & Lee, K. (2002). Imaging skin pathology with polarized light. *J. Biomed. Opt., 7* (3), 329-340.

Jacques, S. L., Ostermeyer, M. R., Wang, L., & Stephens, D. V. (1996). Polarized light transmission through skin using video reflectometry: toward optical tomography of superficial tissue layers. *Proc. SPIE, 2671* (1), 199-210.

Klenle, A., Forster, F. K., Dlebolder, R., & Hibst, R. (2003). Light propagation in dentin: influence of microstructure on anisotropy. *Phys. Med. Biol 48* (2), N7-N14.

Laing, N. G., & Nowak, K. J. (2005). When contractile proteins go bad: The sarcomere and skeletal muscle disease. *BioEssays, 27* (8), 809-822.

Li, X., Ranasinghesagara, J. C., & Yao, G. (2008). Polarization-sensitive reflectance imaging in skeletal muscle. *Opt. Express, 16* (13), 9927-9935.

Linari, M., Dobbie, I., Reconditi, M., Koubassova, N., Irving, M., Piazzesi, G., & Lombardi, V. (1986). The stiffness of skeletal muscle in isometric contraction and rigor: the fraction of myosin heads bound to actin. *J. Muscle Res. Cell Motil., 7* (44), 339-350.

Liu, G. L., Li, Y., & Cameron, B. D. (2002). Polarization-Based Optical Imaging and Processing Techniques with Application to the Cancer Diagnositics. *Proc. SPIE, 4617*, 208-220.

Lu, S.-Y., & Chipman, R. A. (1996). Interpretation of Mueller matrices based on polar decomposition. *J. Opt. Soc. Am. A, 13* (5), 1106-1113.

Manhas, S., Swami, M. K., Buddhiwant, P., Ghosh, N., Gupta, P. K., & Singh, K. (2006). Mueller matrix approach for determination of optical rotation in chiral turbid media in backscattering geometry. *Opt. Express, 14* (1), 190-202.

Mario, J., & Goudail, F. (2004). Influence of the order of diattenuator, retarder, and polarizer in polar decomposition of Mueller matrices. *Opt. Lett., 29* (19), 2234-2236.

Marquez, G., Wang, L. V., Lin, S.-P., Schwartz, J. A., & Thomsen, S. L. (1998). Anisotropy in the Absorption and Scattering Spectra of Chicken Breast Tissue. *Appl. Opt., 37* (4), 798-804.

McDonald, K. S., Wolff, M. R., & Moss, R. L. (1998). Force-velocity and power-load curves in rat skinned cardiac myocytes. *J. Physiol., 511* (2), 519-531.

Moharam, M. G., & Gaylord, T. K. (1983). Three dimensional vector coupled-wave analysis of planer-grating diffraction. *J. Opt. Soc. Am., 73*, 1105-1112.

Nothdurft, R., & Yao, G. (2006). Applying the polarization memory effect in polarization-gated subsurface imaging. *Opt. Express, 14* (11), 4656-4661.

Ossikovski, R., Martino, A. D., & Guyot, S. (2007). Forward and reverse product decompositions of depolarizing Mueller matrices. *Optics letters, 32* (6), 689-691.

Pasquesi, J. J., Schlachter, S. C., Boppart, M. D., Chaney, E., Kaufman, S. J., & Boppart, S. A. (2006). In vivo detection of exercised-induced ultrastructural changes in genetically-altered murine skeletal muscle using polarization-sensitive optical coherence tomography. *Opt. Express, 14* (4), 1547-1556.

Press, W. H., Flannery, B. R., Teukolosky, S. A., & Vetterling, W. T. (1992). *Numerical recipes in C: The art of scientific computing* (2nd.). Cambridge: Cambridge University Press, 1020p.

Rakovic, M. J., & Kattawar, G. W. (1998). Theoretical analaysis of polarization patterns from incoherent backscattering of light. *Appl. Opt., 37* (15), 3333-3338.

Ranasinghesagara, J., & Yao, G. (2007). Imaging 2D optical diffuse reflectance in skeletal muscle. *Opt. Express, 15*, 3998-4007.

Roccoa, H. O. D., Iriartea, D. I., Pomaricoa, J. A., & Ranea-Sandovala, H. F. (2008). Light transmittance in turbid media slabs used to model biological tissues; scaling laws. *Optik-Opt. Int. J. Light Electron. Opt., In Press, Corrected Proof*.

Sankaran, V., Walsh, J. T., & Maitland, D. J. (2000). Polarized light propagation through tissue phantoms containing densely packed scatterers: errata. *Opt. Lett., 25* (12), 933-933.

Sankaran, V., Walsh, J. T., & Maitland, D. J. (2002). Comparative study of polarized light propagation in biologic tissues. *J. Biomed. Opt., 7* (3), 300-306.

Schwartz, C., & Dogariu, A. (2008). Backscattered polarization patterns determined by conservation of angular momentum. *J. Opt. Soc. Am. A, 25* (2), 431-436.

Shukla, P., Awasthi, A., Pandey, P. K., & Pradhan, A. (2008). Discrimination of Normal and Dysplasia in cervix tissue by Mueller Matrix Analysis. *Proc. SPIE, 6864*.

Shurcliff, W. A., & Ballard, S. S. (1964). *Polarized Light*. Princeton: Van Nostrand, 259p.

Sidick, E., Knoesen, A., Xian, J. K., Yeh, Y., & Baskin, R. J. (1992). Rigorous Analysis of Light Diffraction by a Striated Muscle Fibre. *Proc. Biol. Sci., 249* (1326), 247-257.

Smith, M. H. (2001). Interpreting Mueller matrix images of tissues. *Proc. SPIE, 4257*, 82-89.

Swami, M. K., Manhas, S., Buddhiwant, P., Ghosh, N., Uppal, A., & Gupta, P. K. (2006). Polar decomposition of 3 x 3 Mueller matrix: a tool for quantitative tissue polarimetry. *Opt. Express, 14* (20), 9324-9337.

Thornhill, R. A., Thomas, N., & Berovic, N. (1991). Optical diffraction by well ordered muscle fibers. *Eur. Biophys., 20*, 87-99.

Tuchin, V. V., Wang, L. V., & Zimnyakov, D. A. (2006). *Optical Polarization in Biomedial Applications*. Berlin: Springer, 281p.

van Staveren, H. J., Moes, C. J. M., van Marle, J., Prahl, S. A., & van Gemert, M. J. C. (1991). Light scattering in Intralipid-10% in the wavelength range of 400-1100 nm. *Appl. Opt., 30* (31), 4507-4514.

Wang, X., Yao, G., & Wang, L. V. (2002). Monte Carlo model and single-scattering approximation of the propagation of polarized light in turbid media containing glucose. *Appl. Opt., 41* (4), 792-801.

Wyatt, P. J., & Phillips, D. T. (1972). Structure of single bacteria from light scattering. *Journal of Theoretical Biology, 37* (3), 493-501.

Xia, J. (2007). *Optical characterization of skeletal muscles.* University of Missouri, 131.

Xia, J., Weaver, A., Gerrard, D. E., & Yao, G. (2006). Monitoring sarcomere structure changes in whole muscle using diffuse light reflectance. *J. Biomed. Opt., 11* (4), 040504.

Yao, G., & Wang, L. V. (1999). Two-dimensional depth-resolved Mueller matrix characterization of biological tissue by optical coherence tomography. *Opt. Lett., 24* (8), 537-539.

Yao, G., & Wang, L. (2000). Propagation of polarized light in turbid media: simulated animation sequences. *Opt. Express, 7*, 198-203.

Yeh, Y., Baskin, R. J., Lieber, R. L., & Roos, K. P. (1980). Theory of light diffraction by single skeletal muscle fibers. *Biophys. J, 29* (3), 509-522.

Zijp, J. R., & ten Bosch, J. J. (1998). Optical properties of bovine muscle tissue in vitro; a comparison methods. *Phys. Med. Biol., 43* (10), 3065-3081.

VITA

Xin Li was born November, 10, 1984 in Tangshan, Hebei, China. She received her B.S. degree in Optics from Huazhong University of Science and Technology, Wuhan, Hubei, China, in 2007. In fall 2007, she enrolled in the Biological Engineering department of the University of Missouri to pursue her master degree focusing on tissue optics.